Geophysical Journal International

Geophys. J. Int. (2016) **204,** 457–479
GJI Seismology

doi: 10.1093/gji/ggv452

Imaging the transition from flat to normal subduction: variations in the structure of the Nazca slab and upper mantle under southern Peru and northwestern Bolivia

Alissa Scire,[1] George Zandt,[1] Susan Beck,[1] Maureen Long,[2] Lara Wagner,[3] Estela Minaya[4] and Hernando Tavera[5]

[1] *University of Arizona, Tucson, AZ, USA. E-mail: ascire@email.arizona.edu*
[2] *Yale University, New Haven, CT, USA*
[3] *Carnegie Institution of Washington, Washington, DC, USA*
[4] *El Observatorio San Calixto, La Paz, Bolivia*
[5] *El Instituto Geofísico del Perú, Lima, Peru*

Accepted 2015 October 15. Received 2015 July 27; in original form 2015 March 11

SUMMARY

Two arrays of broad-band seismic stations were deployed in the north central Andes between 8° and 21°S, the CAUGHT array over the normally subducting slab in northwestern Bolivia and southern Peru, and the PULSE array over the southern part of the Peruvian flat slab where the Nazca Ridge is subducting under South America. We apply finite frequency teleseismic *P*- and *S*-wave tomography to data from these arrays to investigate the subducting Nazca plate and the surrounding mantle in this region where the subduction angle changes from flat north of 14°S to normally dipping in the south. We present new constraints on the location and geometry of the Nazca slab under southern Peru and northwestern Bolivia from 95 to 660 km depth. Our tomographic images show that the Peruvian flat slab extends further inland than previously proposed along the projection of the Nazca Ridge. Once the slab re-steepens inboard of the flat slab region, the Nazca slab dips very steeply (∼70°) from about 150 km depth to 410 km depth. Below this the slab thickens and deforms in the mantle transition zone. We tentatively propose a ridge-parallel slab tear along the north edge of the Nazca Ridge between 130 and 350 km depth based on the offset between the slab anomaly north of the ridge and the location of the re-steepened Nazca slab inboard of the flat slab region, although additional work is needed to confirm the existence of this feature. The subslab mantle directly below the inboard projection of the Nazca Ridge is characterized by a prominent low-velocity anomaly. South of the Peruvian flat slab, fast anomalies are imaged in an area confined to the Eastern Cordillera and bounded to the east by well-resolved low-velocity anomalies. These low-velocity anomalies at depths greater than 100 km suggest that thick mantle lithosphere associated with underthrusting of cratonic crust from the east is not present. In northwestern Bolivia a vertically elongated fast anomaly under the Subandean Zone is interpreted as a block of delaminating lithosphere.

Key words: Tomography; Seismic tomography; Subduction zone processes; Dynamics of lithosphere and mantle; South America.

INTRODUCTION AND BACKGROUND

The Nazca-South America subduction zone in northern Bolivia and southern Peru is characterized by a change in the upper plate structure, from a narrower orogen in the north to the broad Central Andean Plateau (CAP), typically defined as the region above 3 km elevation, in the south. The northern part of the CAP, the Altiplano plateau, is an internally drained basin characterized by relatively flat, although high, topography with an average elevation of ∼3.5 km (Isacks 1988; Whitman *et al.* 1996). The edges of the Altiplano are defined by the modern active volcanic arc in the west, the Western Cordillera, and a fold and thrust belt in the east, the Eastern Cordillera (Fig. 1a).

The timing and cause of the development of the CAP is debated, with some studies arguing for gradual uplift of the plateau due to shortening and thickening of the crust between 40–30 and 10 Ma based on structural reconstructions (e.g. Elger *et al.* 2005; McQuarrie *et al.* 2005; Oncken *et al.* 2006; Lamb 2011) while

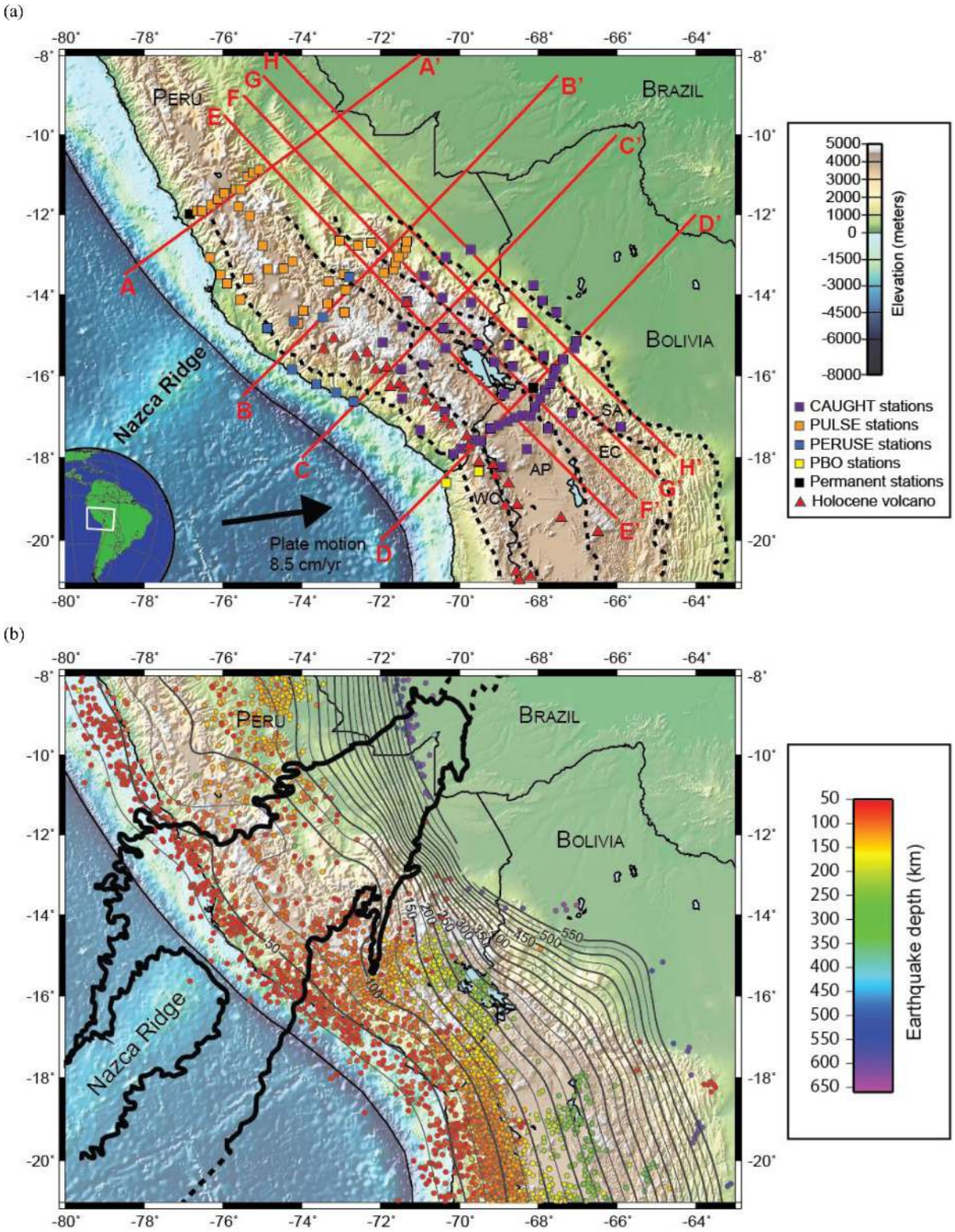

Figure 1. (a) Map showing seismic station locations for CAUGHT and PULSE networks as well as additional stations used in the study and topography of the central Andes. Boundaries of geomorphic provinces (dashed lines) are modified from Tassara (2005). WC, Western Cordillera; AP, Altiplano; EC, Eastern Cordillera; SA, Subandean Zone. Red triangles mark location of Holocene volcanoes (Siebert & Simkin 2002). Plate motion vector is from Somoza & Ghidella (2012). Cross-sections lines (red) are shown for cross-sections in Figs 5, 9, 10 and 11. Solid black line to the west of the coast marks the location of the Peru–Chile trench. (b) Map of seismicity (depth > 50 km, magnitude > 4) and Nazca slab depth contours. Solid black line to the west of the coast marks the location of the Peru–Chile trench. Slab contours (grey) are from the Slab1.0 global subduction zone model (Hayes *et al.* 2012). Earthquake data are from 1973 to 2012; U.S. Geological Survey—National Earthquake Information Center (NEIC) catalogue. Projection of the Nazca Ridge (black) modified from Hampel (2002), based on the conjugate feature in the western Pacific, the Tuamotu Plateau.

paleoelevation studies (e.g. Ghosh *et al.* 2006; Garzione *et al.* 2008) argue for a rapid period of uplift since 10 Ma resulting from large-scale delamination of the lithosphere. Work by Saylor & Horton (2014) using volcanic glasses indicates that uplift of the plateau may have been spatially and temporally non-uniform. This leads them to conclude that the uplift of the plateau could be linked to locally varying crustal shortening or localized removal of mantle lithosphere rather than uniform shortening along the entire plateau or large-scale delamination of the lithosphere. Local delamination of the lithosphere has been proposed in several regions of the Andes using both geochemical (e.g. Kay & Kay 1993; Kay *et al.* 1994; Kay & Coira 2009) and seismic evidence. Seismic observations include both the presence of fast velocity anomalies in the mantle, hypothesized to be delaminated blocks of lithosphere (Asch *et al.* 2006; Koulakov *et al.* 2006; Schurr *et al.* 2006; Bianchi *et al.* 2013; Beck *et al.* 2015), and anomalously low velocities at the base of the crust, which are interpreted as asthenospheric mantle at shallow depths (Myers *et al.* 1998; Heit *et al.* 2008).

Receiver function studies from the central Andes south of our study region (20°–24°S) indicate that the crustal thickness varies across the Andes (Yuan *et al.* 2000, 2002; Beck & Zandt 2002; Wölbern *et al.* 2009) going from a minimum in the forearc and foreland (∼35 km thick) to maxima of up to 70 km thick in the Western and Eastern Cordilleras. The average crustal thickness observed in the Altiplano is ∼65 km. Similar variations in crustal thicknesses are observed in receiver function studies between 8° and 21°S using data from the CAUGHT and PULSE deployments (Ryan *et al.* 2012; Bishop *et al.* 2013). Fast seismic velocities have been observed in the forearc crust in both local earthquake tomography studies between 21° and 24°S (Graeber & Asch 1999; Koulakov *et al.* 2006; Schurr *et al.* 2006), and in ambient noise tomography along much of the central Andes (Ward *et al.* 2013, 2014), possibly resulting from the presence of plutonic remnants of earlier volcanic arcs. Generally the thick crust of the Altiplano plateau has been imaged with low average crustal *P* and *S* -wave velocities (Swenson *et al.* 2000; Ward *et al.* 2013, 2014). Anomalously high velocities in both the crust and uppermost mantle (<150 km depth) have been observed under the Subandean Zone and have been attributed to underthrusting of Brazilian cratonic lithosphere (Myers *et al.* 1998; Beck & Zandt 2002; Phillips *et al.* 2012; Scire *et al.* 2015). Similar observations of high velocity anomalies near 16°S (Dorbath *et al.* 1993; Dorbath & Granet 1996) and analyses of focal mechanisms further north at ∼11°S (Dorbath *et al.* 1991) are also interpreted as evidence for cratonic underthrusting along much of the central Andes.

The subducted Nazca plate in northern Bolivia and southern Peru undergoes a change in slab dip from the Peruvian flat slab region in the north to the normal, steep slab region south of 14°S (Fig. 1b). Subduction of the Nazca plate occurs at an angle of ∼30° under the central Andes. North of ∼14°S, the Nazca slab subducts at a near horizontal angle for several hundred kilometres inland before resuming a more normal angle of subduction (Cahill & Isacks 1992; Hayes *et al.* 2012). The Nazca plate is ∼45 Ma old when it enters the subduction zone beneath the central Andes (Müller *et al.* 2008) and is converging with the South American plate at 8.5 cm yr^{-1} relative to a stable South American reference frame (Somoza & Ghidella 2012). The steeply subducting Nazca slab between 14° and 30° S has been imaged in the upper mantle by a number of tomography studies (e.g. Heit *et al.* 2008; Bianchi *et al.* 2013; Scire *et al.* 2015). Bianchi *et al.* (2013) used regional and global tomography to constrain the subducting Nazca slab to depths of ∼300 km under the Puna Plateau between 24° and 29°S. They observed some variations in the amplitude of the slab anomaly as well as a disruption of the slab anomaly at ∼26°S between 100 and 200 km depth by a low-velocity anomaly, which they note may be the result of vertical smearing of low-velocity anomalies in the crust down into the mantle, resulting in the discontinuous slab anomaly. Both Heit *et al.* (2008) and Scire *et al.* (2015) noted difficulties resolving the Nazca slab at depths shallower than ∼300 km using teleseismic *P*-wave tomography and used earthquake location data to constrain the location of the slab in order to interpret anomalies in the upper 250 km of the mantle.

Scire *et al.* (2015) and Engdahl *et al.* (1995) observed increases in the thickness of the Nazca slab in the mantle transition zone (MTZ), consistent with at least temporary stagnation of the slab in the MTZ. Similar observations of changes in the thickness of the Nazca slab in the MTZ are observed in global tomography studies (e.g. Bijwaard *et al.* 1998; Fukao *et al.* 2001, 2009; Zhao 2004; Li *et al.* 2008; Zhao *et al.* 2013). Both Engdahl *et al.* (1995), who used teleseismic and regional P phases to image the Andean subduction zone between 5° and 25°S down to ∼1400 km depth, and global tomography studies (e.g. Bijwaard *et al.* 1998; Fukao *et al.* 2001, 2009; Zhao 2004; Li *et al.* 2008; Zhao *et al.* 2013) observe that the Nazca slab continues subduction into the lower mantle, although the high velocity anomaly associated with the slab becomes more amorphous in this region.

The flat slab segment in Peru was first identified by Barazangi & Isacks (1976, 1979) although the exact geometry was a matter of some debate (e.g. Snoke *et al.* 1977; Hasegawa & Sacks 1981; Boyd *et al.* 1984). Flat slab subduction is thought to be influenced by the subduction of overthickened oceanic crust although other factors, including the relative motion of the upper plate, also appear to contribute (Gutscher *et al.* 2000; van Hunen *et al.* 2002; Espurt *et al.* 2008; Martinod *et al.* 2013). However, the importance of the subduction of overthickened oceanic crust relative to other factors in the development of flat slab subduction is debated (e.g. van Hunen *et al.* 2004; Gerya *et al.* 2009; Skinner & Clayton 2013; Phillips & Clayton 2014). Regions of flat slab subduction are characterized by the absence of volcanism as the decreasing dip of the slab displaces the mantle wedge, preventing the hydrated subducted crust from having contact with hot asthenospheric mantle and therefore precluding partial melting of the mantle and the associated volcanism (Isacks & Barazangi 1977; Gutscher 2002).

North of 14°S, the Nazca slab subducts horizontally at about 100 km depth for several hundred kilometres inland (Cahill & Isacks 1992; Hayes *et al.* 2012; Phillips & Clayton 2014). However, the exact geometry of the Peruvian flat slab is uncertain due to the limited slab seismicity (Fig. 1b). The Peruvian flat slab region corresponds to a gap in Andean arc volcanism. The modern volcanic arc, the Western Cordillera, is active up to around 14°S where volcanism is shut off by the Peruvian flat slab segment (McGeary *et al.* 1985). The southern end of the flat slab segment near 14°S is bounded by the Nazca Ridge, a bathymetric high on the Nazca plate thought to have been formed by the Easter-Salas hotspot (see Ray *et al.* 2012 and references therein for a complete discussion of the origin of the Nazca Ridge). The oceanic crustal thickness of the Nazca Ridge is estimated to be between 15 and 18 km from Rayleigh wave dispersion curve modelling (Woods & Okal 1994) and offshore seismic reflections studies (Hampel *et al.* 2004). The Peruvian flat slab extends ∼1500 km to the northwest, steepening near the Grijalva Fracture Zone at ∼5°S. The subduction of a large oceanic plateau, termed the Inca Plateau, which is theorized to be the conjugate feature of the Marquesas Plateau in the western Pacific is proposed as an explanation for the lateral extent of the Peruvian

flat slab (Gutscher *et al.* 1999b). Subduction of this hypothetical plateau may support flat subduction in the northern section of the Peruvian flat slab, although Skinner & Clayton (2013) argue that the Inca Plateau has subducted too far to the east to continue supporting the flat slab.

Reconstructions of the migration history of the Nazca Ridge initially indicated that the Nazca Ridge entered the trench at 8 Ma at 8°S (von Huene *et al.* 1996). A more recent reconstruction by Hampel (2002) using comparisons with the Tuamotu Plateau, the conjugate feature of the Nazca Ridge in the western Pacific, concludes that the Nazca Ridge entered the trench at ∼11°S at about 11 Ma. The oblique angle of the Nazca Ridge to the trench and the plate convergence direction results in migration of the ridge south along the margin although estimates of the rate of southward migration vary between studies. Arc volcanism appears to have shut off at ∼4 Ma above the present day location of the Nazca Ridge (Rosenbaum *et al.* 2005), indicating that the subducting slab flattened in this region around the end of the Miocene.

Although some regions of flat slab subduction have been extensively studied, particularly the Pampean flat slab segment in central Chile (e.g. Gans *et al.* 2011; Porter *et al.* 2012; Burd *et al.* 2013; Marot *et al.* 2014) the effect of along strike changes in slab dip on the deformation pattern of the subducting plate are not completely understood. As the angle of subduction changes along strike, the subducting plate is forced to bend and deform to accommodate the change in subduction angle. This change in subducting plate geometry has the potential to result in thinning or even tearing of the subducting slab between regions of steep and flat subduction. Mantle flow patterns would be affected by the geometry of the subducting slab, particularly if tearing of the slab occurs. Eakin & Long (2013) observe trench-normal fast shear wave splitting directions under the Peruvian flat in the subslab mantle, which shift to trench-oblique fast splitting directions to the south under the normally dipping slab. Changes in splitting directions are also observed in the mantle above the flat slab to the north and south of the Nazca Ridge (Eakin *et al.* 2014). This implies that the flat slab is influencing mantle deformation and flow both above and below the Nazca slab. Slab tears are postulated further north in the Andes beyond the northern edge of the Peruvian flat slab where the Carnegie Ridge is subducting near 1°S (Gutscher *et al.* 1999a). Evidence for slab tearing related to Carnegie Ridge subduction includes variations in volcano geochemistry and upper-mantle focal mechanisms. However, studies above the Pampean flat slab in central Chile indicate that while mantle flow patterns are being affected by the shallowing of the slab, the slab bends in the mantle as the slab geometry shifts from normal to flat subduction rather than tearing (Anderson *et al.* 2004). A slab tear has been hypothesized on the southern edge of the Peruvian flat slab as a result of the abrupt change in slab dip (e.g. Barazangi & Isacks 1979), but later studies based on slab seismicity (e.g. Hasegawa & Sacks 1981; Schneider & Sacks 1987; Kumar *et al.* 2014; Dougherty & Clayton 2015) and receiver functions (Phillips & Clayton 2014) indicate that the change in slab dip south of the Nazca Ridge is accommodated by bending of the slab rather than a tear above 200 km depth. Recent work using receiver functions (Bishop *et al.* 2013) and earthquake surface wave tomography (Knezevic Antonijevic *et al.* 2015) have proposed the possibility of a shallow, trench parallel tear above 100 km depth to the north side of the Nazca ridge.

We deployed two arrays of seismic stations, the CAUGHT array in northwestern Bolivia and southern Peru, and the PULSE array which was deployed over the southern part of the Peruvian flat slab, to investigate the structure of the mantle and the subducting Nazca plate in this region (Fig. 1a). We use finite frequency teleseismic *P*- and *S*-wave tomography to image the mantle from depths of 95 km to the base of the MTZ between 8° and 21°S to explore variations in upper-mantle structure and to try to better constrain the geometry of the subducting Nazca slab. This study offers further insights into how the Altiplano and the Andean system interact with the mantle below by presenting new tomography images of the Andean mantle above the normally dipping slab under the central Andes. In addition, constraining the Nazca slab under northwestern Bolivia and southern Peru in the transition between flat and normal subduction allows us investigate the effects of flat subduction on the deformation and geometry of the subducting slab.

DATA

The data set assembled for this study was collected from 99 broadband seismometers deployed in northwestern Bolivia and southeastern Peru between 2010 and 2013 (Fig. 1a). The CAUGHT deployment includes 48 stations in Bolivia and Peru (Beck *et al.* 2010). The PULSE deployment consists of an additional 38 stations deployed in Peru, primarily over the southern part of the Peruvian flat slab (Wagner *et al.* 2010). An additional eight stations from the PeruSE deployment (Phillips *et al.* 2012), including four stations along the coast of Peru, and three stations from the permanent Plate Boundary Observatory network (Sodoudi *et al.* 2011) in Chile were included to improve coverage of the study area. Also included are two permanent stations, LPAZ and NNA, from the Global Telemetered Seismic Network and the Global Seismograph Network respectively.

Arrival times were picked for direct *P* phases for 150 earthquakes with magnitudes greater than 5.0 between 30° and 90° away from the study region. Additional arrivals were picked for PKIKP phases for 85 earthquakes with a similar magnitude limit between 155° and 180° away from the study region (Fig. 2a). *S*-wave data were rotated to the radial and tangential components and direct *S*-wave arrivals were picked on the tangential component for 144 earthquakes with magnitudes greater than 5.0 between 30° and 90° away from the study region (Fig. 2c). Similar to our previous study (Scire *et al.* 2015), first arrivals were picked using the multi-channel cross correlation technique described by VanDecar & Crosson (1990) and modified by Pavlis & Vernon (2010). 14 124 direct *P* and 6889 PKIKP arrivals were picked in three frequency bands with corner frequencies 0.2 to 0.8 Hz, 0.1 to 0.4 Hz and 0.04 to 0.16 Hz. Distribution of the picks in the three frequency bands is dominated by the 0.2 to 0.8 Hz band, with 48.93 per cent of all picks in the 0.2 to 0.8 Hz band, 27.10 per cent in the 0.1 to 0.4 Hz band and 23.97 per cent in the 0.04 to 0.16 Hz band. 6014 direct S arrivals were also picked in three frequency bands with corner frequencies 0.1 to 0.7 Hz, 0.04 to 0.16 Hz and 0.01 to 0.09 Hz. The S arrivals are fairly evenly split between the 0.01 to 0.09 Hz band and the 0.04 to 0.16 HZ band with 48.84 per cent of all picks occurring in the 0.01 to 0.09 Hz band and 40.90 per cent in the 0.04 to 0.16 Hz band. Relatively few high quality S arrivals were observed in the highest frequency band with only 10.26 per cent of all picks occurring in the 0.1 to 0.7 Hz band.

Back azimuthal distribution of incoming rays for both the *P*- and *S*-waves (Figs 2b and d) is uneven, with the majority of rays coming from direct *P* and direct *S* phases from earthquakes either in the Middle America subduction zone to the northwest or the South Sandwich Islands subduction zone to the southeast. This bimodal distribution is further emphasized by the limited number of usable events to the east of our study region on the Mid-Atlantic Ridge.

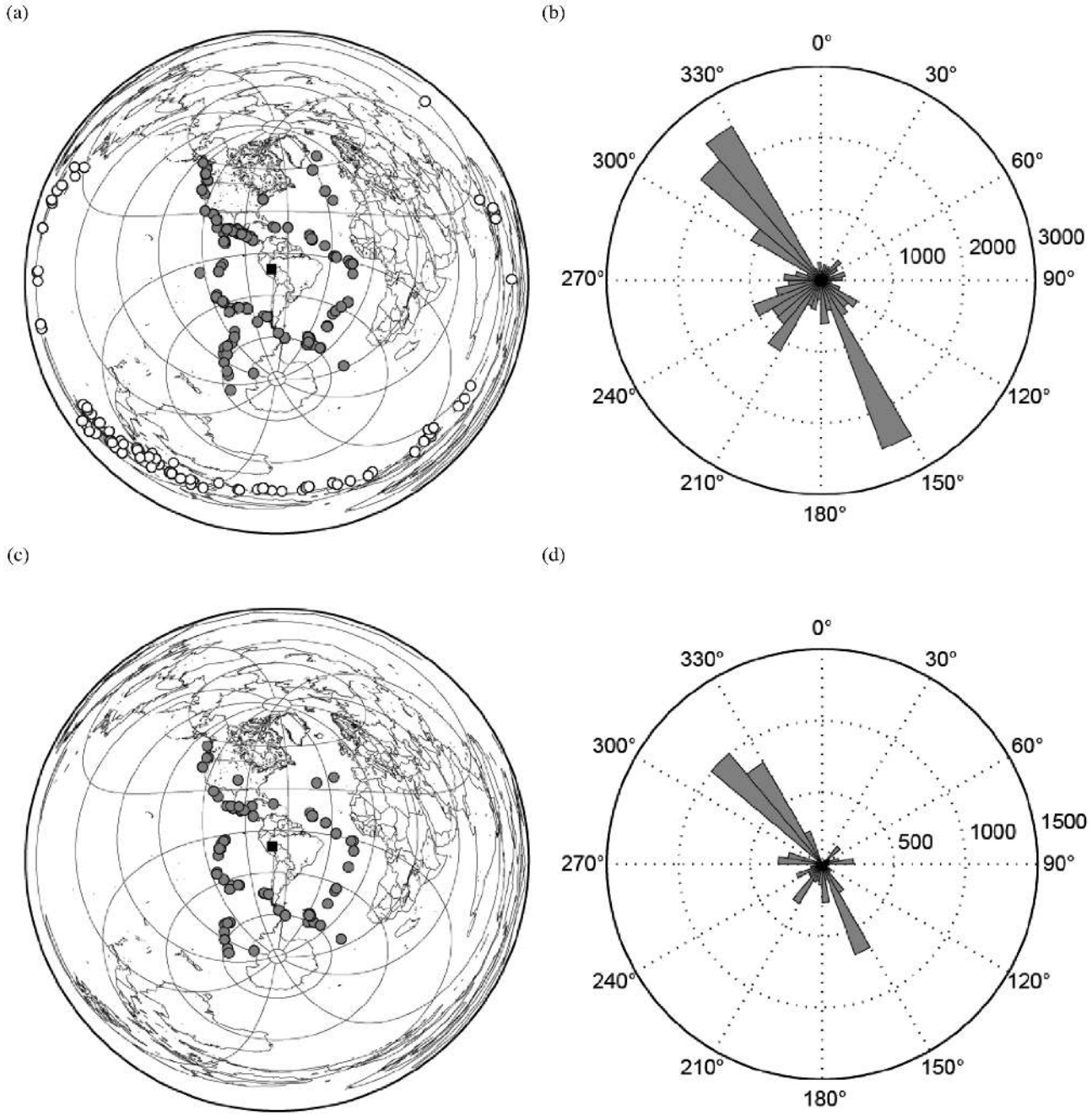

Figure 2. (a) Global map centred on our study region (black square) showing the location of *P*-wave events used in this study. Darker grey circles mark events used for direct *P* arrivals while open circles mark events used for PKIKP arrivals. (b) Plot showing the azimuthal distribution for all rays used for *P*-waves in the study. Ray distribution is strongly controlled by the location of plate boundaries where the earthquakes are generated. (c) Global map centred on our study region (black square) showing the location of *S*-wave events used in this study. (d) Plot showing the azimuthal distribution for all rays used for *S*-waves in the study. Ray distribution is strongly controlled by the location of plate boundaries where the earthquakes are generated.

Travel time residuals were calculated relative to IASP91 (Kennett & Engdahl 1991). The residuals were then demeaned for each event to determine the relative travel time residuals.

Travel times were corrected for crustal variations using Moho depth estimates from receiver functions from Bishop *et al.* (2013) and Ryan *et al.* (2012). Given that information on crustal structure in our study region is limited, crustal corrections were made using a homogenous layered velocity model corresponding to the average velocity of the central Andean crust (Zandt *et al.* 1996; Dorbath & Masson 2000; Swenson *et al.* 2000). Crustal corrections for stations in the forearc were calculated using higher crustal velocities based on local tomography studies from further south (Graeber & Asch 1999; Koulakov *et al.* 2006; Schurr *et al.* 2006) and ambient noise tomography, which covers part of our study region (Ward *et al.* 2013, 2014).

METHOD

This study uses a finite-frequency teleseismic tomography algorithm discussed in detail by Schmandt & Humphreys (2010) and

used in our previous study (Scire *et al.* 2015). The finite-frequency approximation defines the sampled area around the geometrical ray path by the first Fresnel zone, whose width is dependent on both the frequency and the distance along the ray path (Dahlen *et al.* 2000; Hung *et al.* 2000). The sampling in each model layer is determined by the width of the Fresnel zone, which increases with distance from the source or receiver, and the differential sensitivity within the Fresnel zone, resulting in theoretical 'banana-doughnut' sensitivity kernels (Dahlen *et al.* 2000). A detailed discussion of the specific algorithm used to calculate the sensitivity kernels can be found in Schmandt & Humphreys (2010). Multiple nodes in each model layer are sampled by these sensitivity kernels for a single arrival, increasing sampling of the model space over tomography algorithms that assume that sampling occurs only along the theoretical ray path.

The model space is parametrized as a series of nodes in a non-uniform grid that dilates with increasing depth and distance from the centre of the model as in Scire *et al.* (2015). In the shallowest layers of the model in the centre where sampling is densest, the horizontal nodes are spaced 35 km, increasing to 56 km at the edges of the model. Vertical node spacing increases with depth, from 35 km at 60–95 km depth to 55 km at depths greater than 555 km. The horizontal node spacing also increases with depth, with nodes in the centre of the model increasing from 35 km spacing in the shallowest model layers to 49 km in the deepest model layers. Node spacing on the outer edges of the model increases from 56 km in the shallowest model layers to 78 km in the deepest model layers. The sampling of the model space was determined by calculating normalized hit quality maps in which each node is assigned a hit quality value between 0 and 1 that is a function of both the number of rays sampling that node as well as the azimuthal distribution of those rays (Supporting Information Figs S1 and S2; Schmandt & Humphreys 2010; Biryol *et al.* 2011; Scire *et al.* 2015). Nodes that are not sampled are assigned a hit quality of 0 while nodes that are sampled by multiple rays from all four geographical quadrants are assigned a hit quality of 1.

The inverse problem is regularized using norm and gradient damping, details of which are discussed in Schmandt & Humphreys (2010). In addition, smoothing is applied to the sensitivity kernels to account for uncertainties in the location of the ray paths. We also incorporate station and event terms in order to compensate for perturbations outside of the model space. Since our crustal thickness corrections are calculated using a homogenous layered velocity model, the station terms account for local perturbations in the velocity structure that are not accounted for in the crustal corrections as well as any errors in the a priori crustal thickness. The event terms account for variations in mean velocity structure under the subset of stations that record a specific event. As in Scire *et al.* (2015), the uppermost model layer (60 km) and the lowermost model layer (715 km) are not interpreted because these layers also absorb effects from anomalies outside of the model space that are not accounted for in the crustal corrections or the global mantle velocity model, respectively. Sampling of the shallowest and deepest model layers is also limited by the station locations and the spreading of the ray paths respectively. We use the LSQR algorithm of Paige & Saunders (1982) to invert the frequency-dependent relative travel time residuals in order to obtain velocity perturbations within the modelled volume. This algorithm aims to obtain the minimum energy/length model that satisfactorily explains the observed data. We performed a trade-off analysis between the variance reduction and the Euclidean model norm to choose the overall damping and smoothing weights (Supporting Information Fig. S3). Using the chosen damping (6) and smoothing (5) parameters for both the *P*- and *S*-wave inversions results in variance reductions of 83.5 per cent and 82.7 per cent respectively.

Synthetic resolution tests were performed to determine the ability of our model to resolve mantle structures (Figs 3 and 4). A synthetic 'checkerboard' input was created with alternating fast and slow velocity anomalies with amplitudes of +5 per cent and −5 per cent respectively for *P*-waves, defined in eight-node cubes (Fig. 3a), and +9 per cent and −9 per cent respectively for *S*-waves, defined in 27-node cubes (Fig. 3b). Larger 'checkers' were used for the *S*-wave synthetic tests due to the decreased resolution of the *S*-wave inversion caused by the more limited number of rays used in the inversion. Resolution of the *S*-wave inversion is also affected by the lower frequency content of the *S*-wave arrivals, resulting in larger Fresnel zones for the *S*-wave inversion (Hung *et al.* 2000). The size and location of the input anomalies varies with depth due to the depth dependent dilation of the node spacing (Fig. 4). In order to determine the extent of any lateral or vertical smearing, the input anomalies are separated by neutral 2-node cubes that contain no velocity anomalies. The output from the checkerboard tests shows that lateral resolution is good in the centre of the model space, with smearing of anomalies increasing towards the edges due to the decrease in the number of crossing rays (Fig. 3). Some vertical smearing of anomalies is observed, resulting in low amplitude anomalies being erroneously resolved into neutral background layers in both the *P*- and *S*-wave resolution tests (Fig. 4 and Supporting Information Fig. S5). The synthetic tests also indicate that there is a loss of amplitude in the output of the checkerboard tests. Only ∼60 per cent of the input amplitude is recovered in the centre of the model space, with amplitude recovery decreasing towards the edges of the model. Similar loss of recovered amplitude occurs with depth, with lower amplitude recovery observed in the centre of the model in the deepest depth slices.

A second set of synthetic tests were performed to determine the ability of the inversion to resolve the subducting Nazca slab, since it is one of the most prominent structures that we expect to observe. The Slab1.0 global subduction zone model (Hayes *et al.* 2012) was used to create a synthetic slab anomaly that is between ∼70–100 km thick with amplitudes of +5 per cent in order to test the ability of the *P*-wave model to resolve the flat slab in the northern part of the study region and the transition to the steeply dipping slab in the south (Fig. 5). As was observed by Scire *et al.* (2015), recovery of the slab anomaly above 200 km is complicated by vertical smearing effects and decreased amplitude recovery. In the northern part of the study region, the recovered amplitude of the shallow, flat anomaly corresponding to the Peruvian flat slab is even more diminished, indicating that we probably cannot image the flat slab segment due to an insufficient number of crossing rays in the shallowest model layers. Below 200 km depth, the recovered slab anomaly is more distinct and increases in amplitude. In the deeper parts of the model, the recovered slab location corresponds well to the input slab location, indicating that we should be able to image the Nazca slab down to 660 km depth. Similar patterns are observed for slab recovery tests for the *S*-wave model for a synthetic slab with amplitude of +9 per cent although less amplitude is recovered for the *S*-wave model especially on the edges of the model.

RESULTS

The results from this study are displayed as horizontal depth slices in Figs 6–8, and vertical cross-sections in Figs 9 and 10. Additional

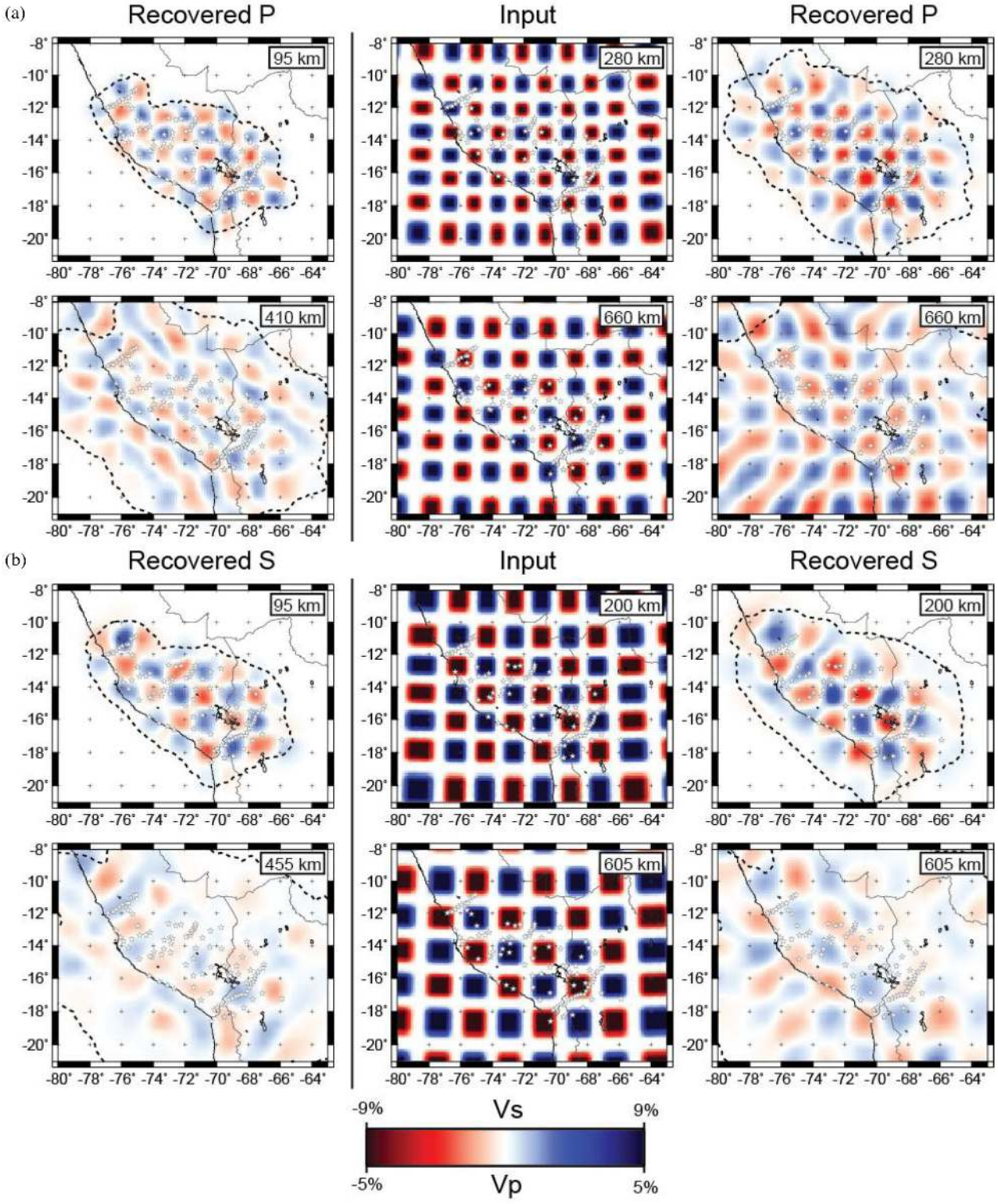

Figure 3. Horizontal depth slices for the checkerboard tests for a selection of model layers. Input for neutral layers (0 per cent velocity deviation) is not shown. Output for neutral layers is shown in the left column. The short dashed line represents the edge of the well-resolved region of the model, defined as regions with hit quality greater than 0.2 (Biryol *et al.* 2011). (a) Checkerboard tests for *P*-wave inversion. The checkerboard tests show that for shallower layers, resolution is controlled by station distribution as expected. Deeper model layers indicate that while the input amplitude cannot be completely resolved, lateral changes in anomalous velocity resolve with little horizontal smearing. Resolution is lost towards the edges of the model region. Resolution of velocity anomalies in neutral layers shown here (left column) indicates that some vertical smearing is occurring. (b) Checkerboard tests for *S*-wave inversion. Larger input 'checkers' are used for *S*-waves due to decreased resolution of *S*-wave inversion relative to *P*-wave inversion. Amplitude recovery for the *S*-wave inversion decreases more rapidly with depth than for the *P*-wave inversion. Resolution of velocity anomalies in neutral layers shown here (left column) indicates that some vertical smearing is occurring. Checkerboard tests for additional model layers are in Supplemental Material Fig. S4.

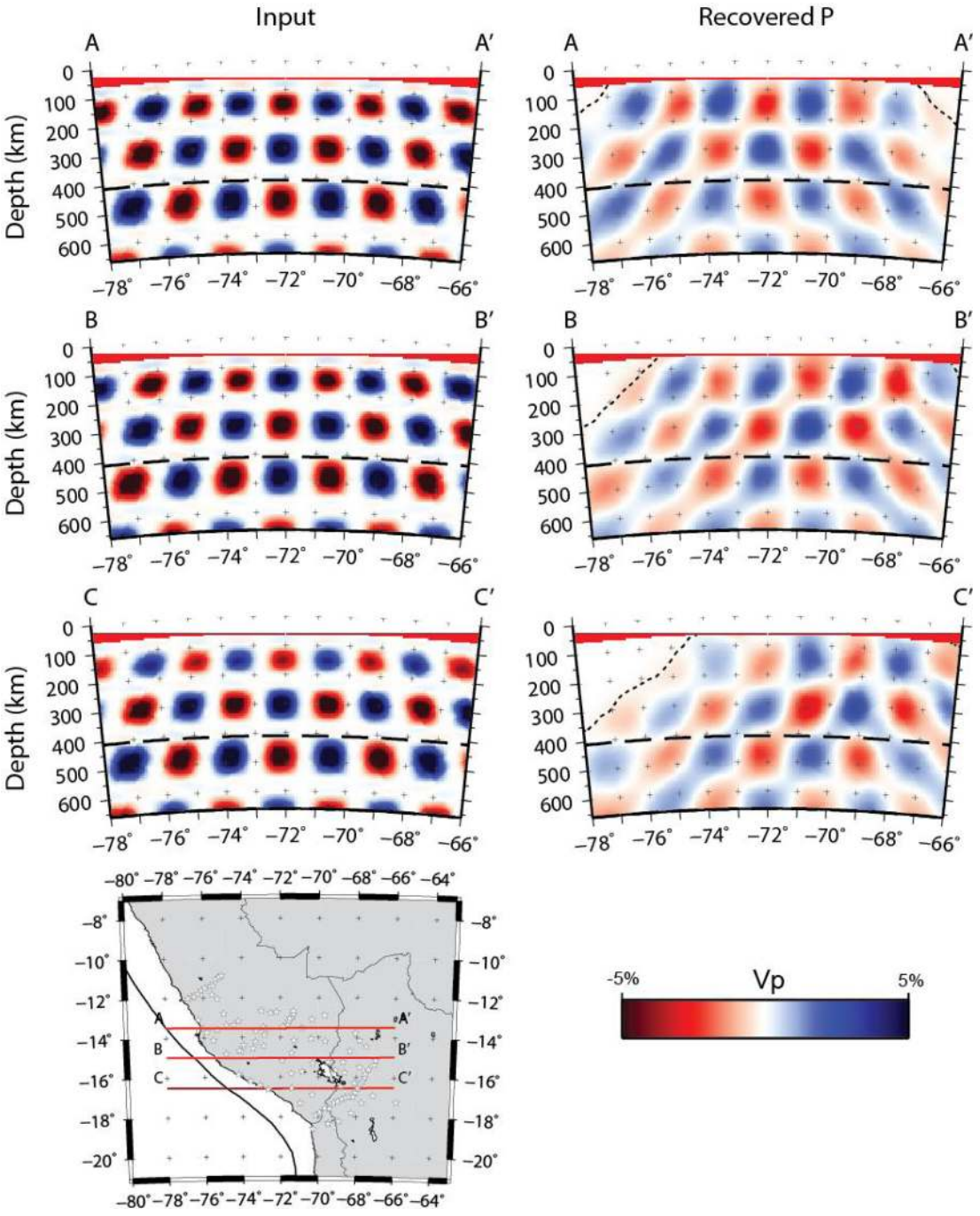

Figure 4. E–W oriented cross-sections through checkerboard tests for *P*-wave inversion. Dashed lines are the same as in Fig. 3. Irregular distribution of anomalies with depth in synthetic input (left) is due to the dilation of the node spacing with depth. Location of cross-sections shown in map in lower left. Cross-sections through the checkerboard tests for the *S*-wave inversion are in Supporting Information Fig. S5.

depth slices and cross-sections are included in the Supporting Information (Supporting Information Figs S9–S11). The model is resolved down to 660 km depth. In the shallowest depth slices, resolution is strongly controlled by the location of the stations. Horizontal resolution is good throughout the model, allowing for the interpretation of lateral differences in mantle structure. At all depths, model resolution decreases towards the edges of the model space. In the northern part of the study area, the shallowest depth slice that we are able to interpret, 95 km, is already within the lithosphere of the Peruvian flat slab, preventing us from making any observations of anomalies above the flat slab.

The Nazca slab

The subducting Nazca slab is the most prominent anomaly we observe in our tomograms. The Nazca slab is observed in both the *P*- and *S*-wave tomograms as a fast anomaly with variable amplitude that migrates northeast with depth (Figs 6–8). Due to the complications in resolving shallow structure discussed previously, identifying the Nazca slab in the shallower parts of the model (particularly 95 to 130 km depth) is difficult (Fig. 6). Furthermore, resolution of the slab anomaly between 130 and 165 km depth below the active volcanic arc in the southern part of our study area is complicated by the

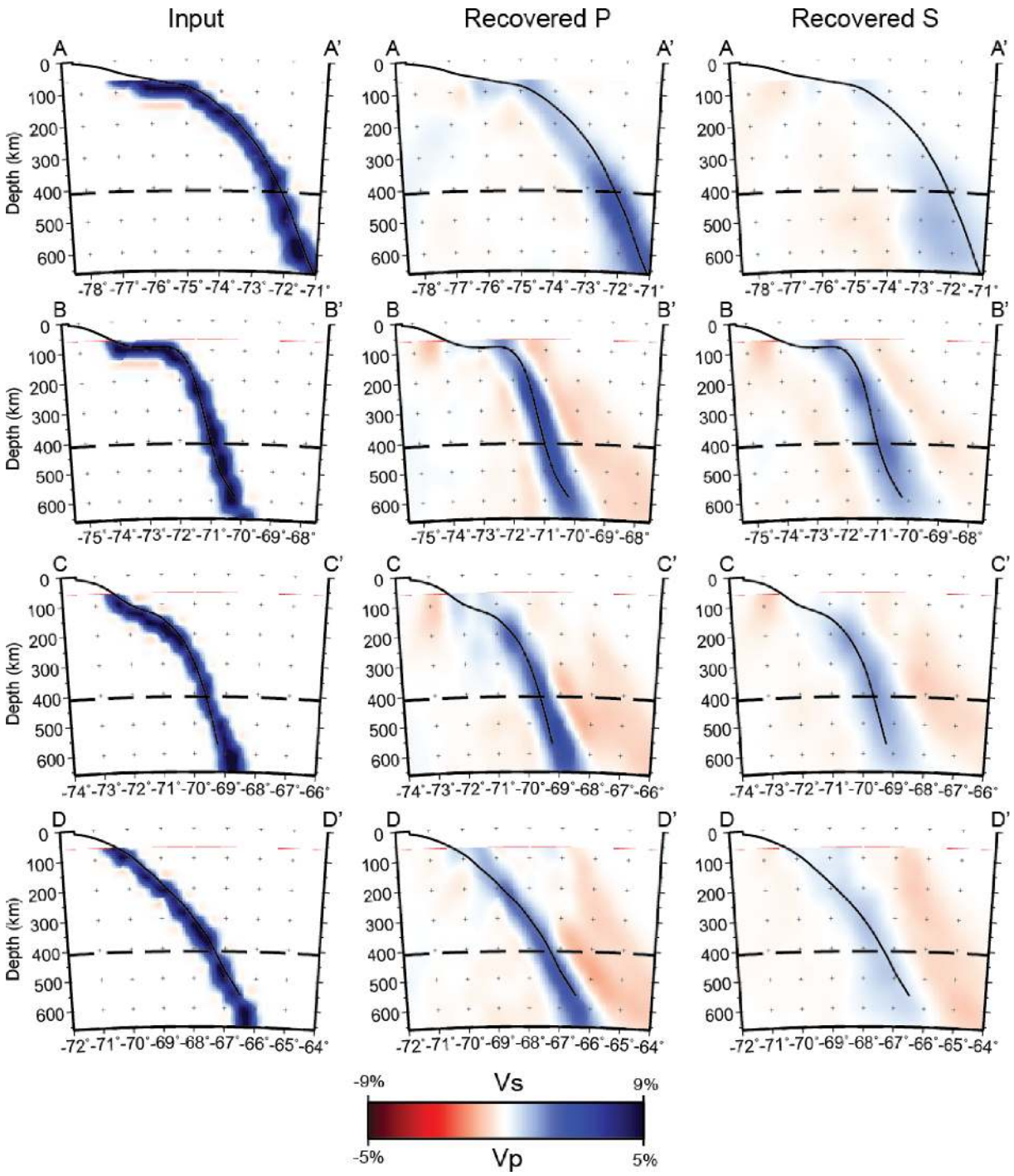

Figure 5. Cross-section results for our synthetic slab recovery tests. Cross-section locations are shown in Fig. 1. The geometry of our input slab model is based on the Slab1.0 contours (black line, Hayes *et al.* 2012). Synthetic input (left), recovered Vp (centre) and recovered Vs (right) models are shown. Decreased amplitude recovery and vertical smearing of the recovered slab anomaly is observed in the upper 200 km of the model. In general, the amplitude recovery increases with depth.

presence of a high-amplitude low-velocity anomaly below the arc (Anomaly B, Figs 6 and 9). Difficulty resolving the slab anomaly in the region where the subduction angle changes from steep to shallow near 14°S is also noted at 95 and 130 km depth, possibly due to interference from high-amplitude low-velocity anomalies both northwest (below) and southeast (above) of the slab. At the northern edge of our study area, a fast anomaly that corresponds to the location of intermediate depth earthquakes between 95 and 165 km depth is noted, although its connection to the slab anomaly to the south is outside of our resolution (Anomaly A, Fig. 6). The slab anomaly becomes more prominent and more continuous at greater depths, allowing us to make observations about the subducting slab down to 660 km depth. For the depth slices at 280 km and 365 km some differences exist in the shape of the Nazca slab relative to the Slab1.0 contours, particularly in the northern half of our study region (Fig. 7). North of ∼16°S the strike of the slab is more

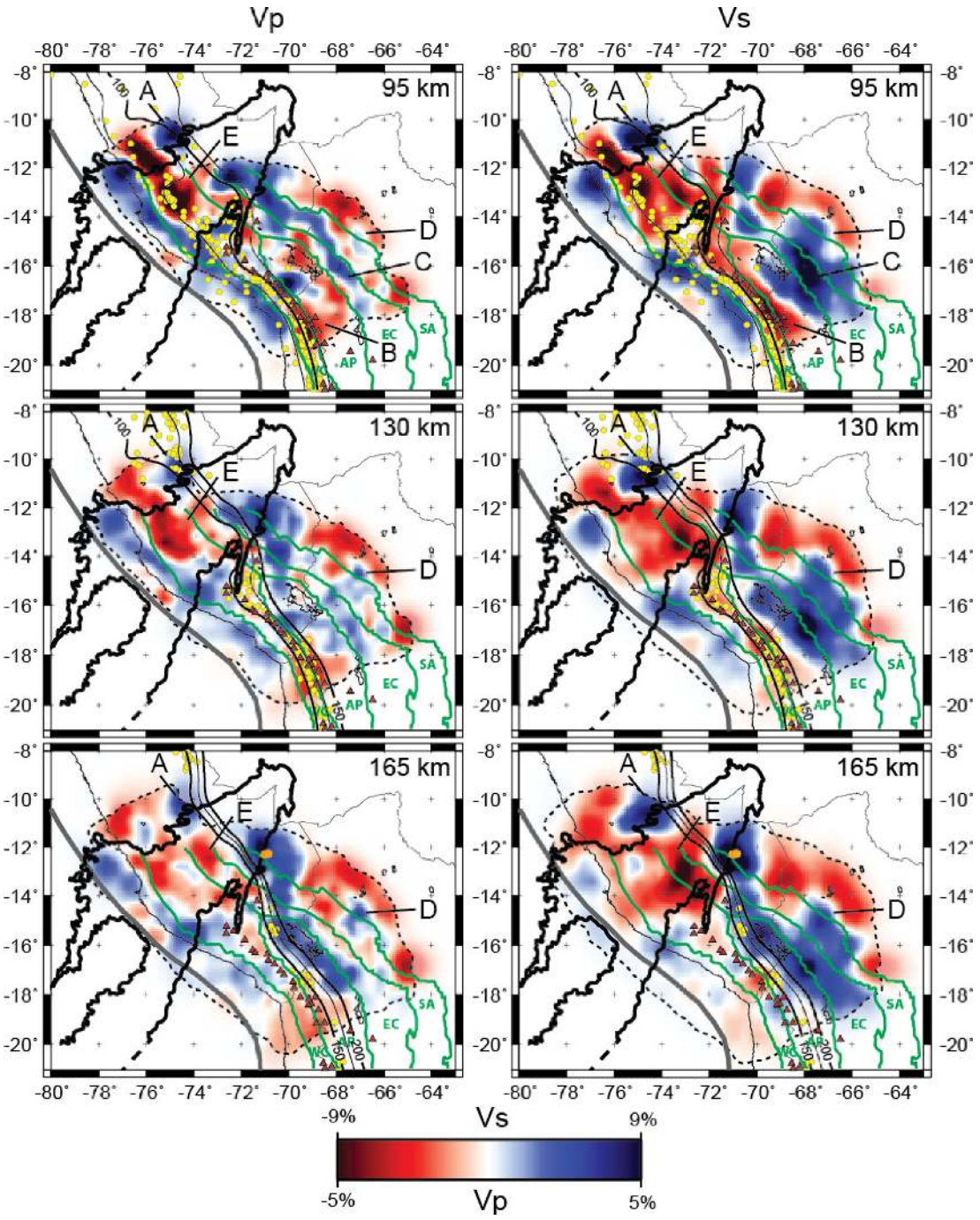

Figure 6. Horizontal depth slices for 95, 130 and 165 km from the tomography model for both Vp (left) and Vs (right). The short dashed line represents the edge of the well-resolved region of the model, defined as regions with hit quality greater than 0.2 (Biryol *et al.* 2011). Geomorphic provinces (green lines) are the same as in Fig. 1(a). Red triangles mark location of Holocene volcanoes (Siebert & Simkin 2002). Yellow dots are earthquake locations from the EHB catalogue (Engdahl *et al.* 1998). Solid black lines are slab contours from Slab1.0 model (Hayes *et al.* 2012). Orange dots mark reflection points from James & Snoke (1990). Thick grey line to the west of the coast marks the location of the Peru–Chile trench. Heavy black outline marks the projection of the subducted Nazca Ridge from Hampel (2002). Labelled anomalies (A, B, C, D and E) are discussed in the text.

north-south than the Slab1.0 contours suggest, and there is a sharp eastward deflection in the slab strike between 15° and 16°S prior to resuming a more north-south orientation following the contours southward. This 'kink' is especially clear in the *S*-wave tomogram at 280 km depth but is less clear in the corresponding *P*-wave image. We note that this part of the slab has very little seismicity, possibly explaining the difference from the Slab1.0 contours, which are constrained mostly by slab seismicity in regions like our study area where limited geophysical work has been done previously. This illustrates the utility of tomograms in offering additional constraints on slab geometry for models like Slab1.0. The slab anomaly shows along-strike variations in amplitude in our tomograms (Figs 7 and 8). A bend in the slab anomaly is observed in the MTZ between 14° and 18°S corresponding to the location of the Bolivian

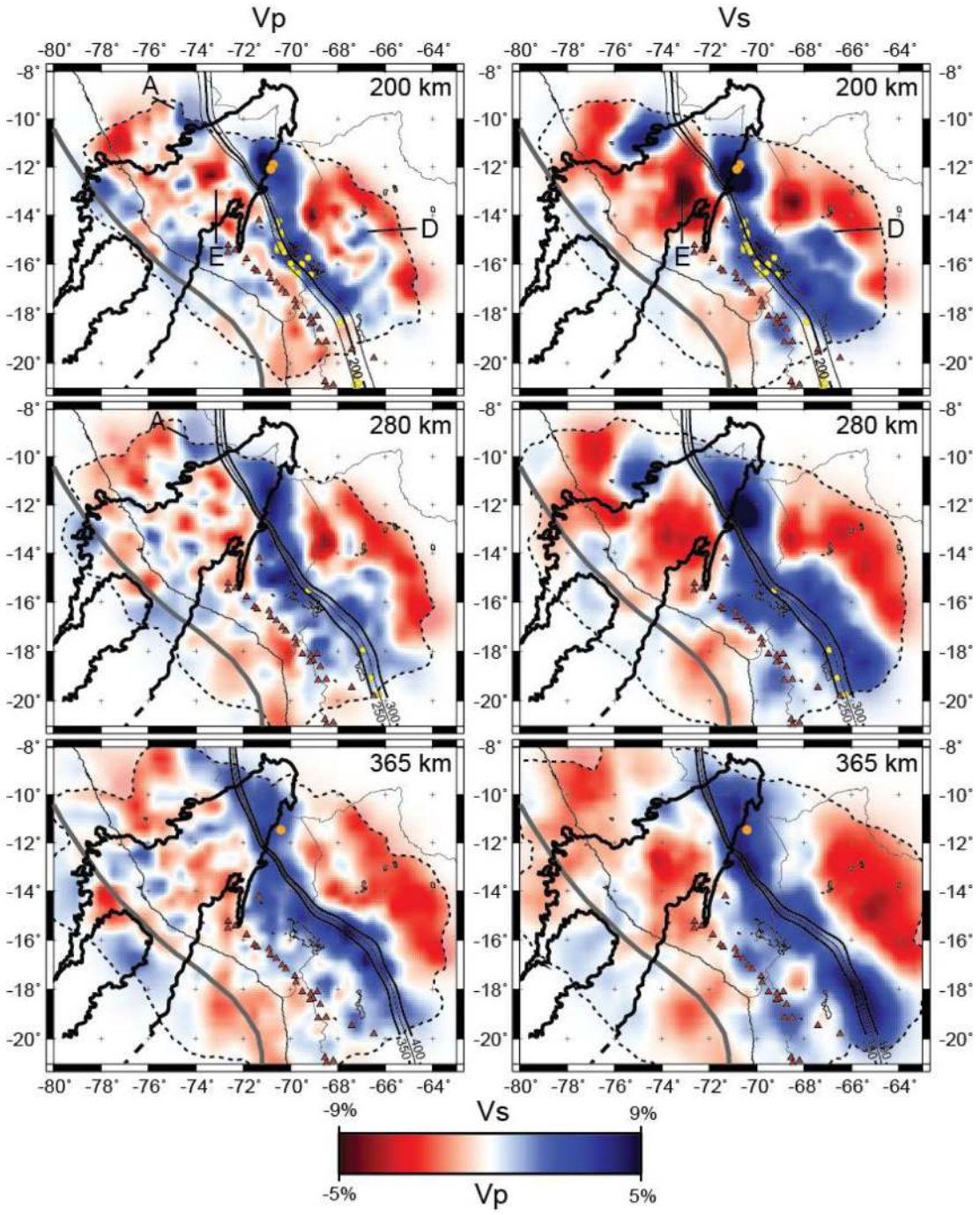

Figure 7. Horizontal depth slices for 200, 280 and 365 km from the tomography model for both Vp (left) and Vs (right). Dashed lines are the same as in Fig. 6. Red triangles mark the location of Holocene volcanoes (Siebert & Simkin 2002). Yellow dots are earthquake locations from the EHB catalogue (Engdahl *et al.* 1998). Solid black lines are slab contours from Slab1.0 model (Hayes *et al.* 2012). Orange dots mark reflection points from James & Snoke (1990). Thick grey line to the west of the coast marks the location of the Peru–Chile trench. Heavy black outline marks the projection of the subducted Nazca Ridge from Hampel (2002). Labelled anomalies (A, D and E) are discussed in the text.

orocline (Fig. 8). North of the bend in the slab anomaly, the fast slab anomaly appears to thicken in the MTZ (compare 410 km depth slice to 605 km depth slice in Fig. 8).

The supra-slab mantle

The uppermost mantle south of 14°S above the normally dipping Nazca slab is highly variable. In the southernmost part of our study area, a −2 per cent slow anomaly in the *P*-wave tomograms is observed under the western Altiplano (Anomaly B, Figs 6 and 9). The corresponding anomaly in the *S*-wave results is much higher amplitude (−6 per cent). This anomaly is confined to the west by the subducting slab and to the northeast by a variable amplitude fast anomaly (Anomaly C, Figs 6, 9 and 10). The shape and size of this fast anomaly (Anomaly C) is highly variable although it appears to be confined to the Eastern Cordillera and Subandean Zone. Slow anomalies are noted to the northeast of this fast anomaly,

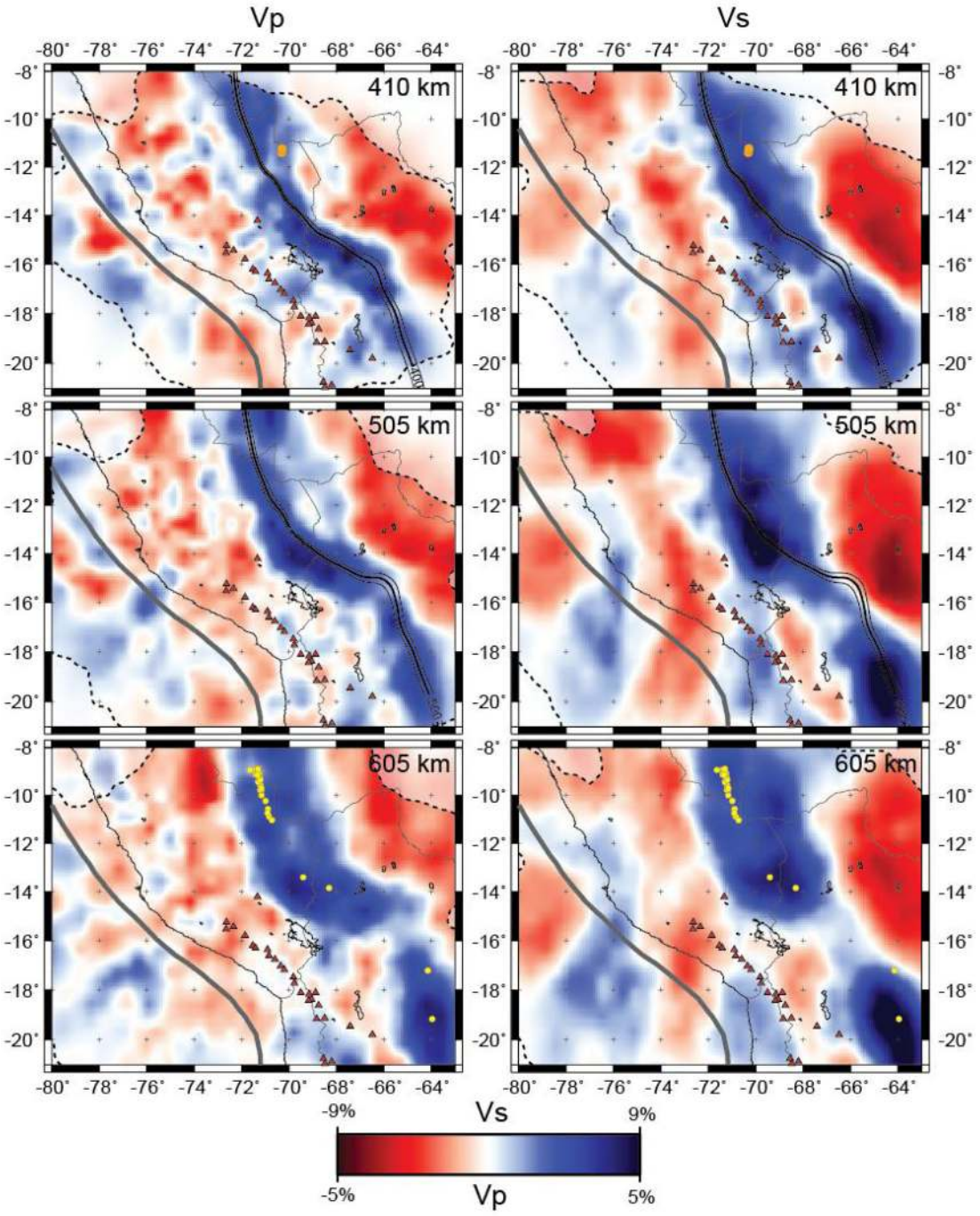

Figure 8. Horizontal depth slices for 410, 505 and 605 km from the tomography model for both Vp (left) and Vs (right). Dashed lines are the same as in Fig. 6. Red triangles mark location of Holocene volcanoes (Siebert & Simkin 2002). Yellow dots are earthquake locations from the EHB catalogue (Engdahl *et al.* 1998). Solid black lines are slab contours from Slab1.0 model (Hayes *et al.* 2012). Orange dots mark reflection points from James & Snoke (1990). Thick grey line to the west of the coast marks the location of the Peru–Chile trench. Additional depth slices are in the Supporting Information Figs S9 and S10.

indicating that its lateral extent is limited. A second fast (+3 per cent) anomaly is noted in the *P*-wave tomograms under the Subandean Zone around 15°S (Anomaly D, Figs 6, 7, 9 and 10). This anomaly extends vertically in the mantle from ∼95 km depth to 200 km depth.

Additional recovery tests were performed to test the ability of our model to resolve anomalies of interest in the shallow mantle (Fig. 11). The initial synthetic model (Fig. 11, left) includes several bodies, reproducing realistic anomalies from our results, combined with the subducting Nazca slab constrained by Slab1.0 as in our slab recovery tests (Fig. 4). The labelled anomalies are C and D located above the slab and anomaly E below the slab discussed in the next section. The synthetic recovery test in Fig. 11 indicates that while the lateral extent of these anomalies is fairly well recovered, vertical smearing of these anomalies makes it difficult to determine the exact vertical extent. In particular, the recovered Anomalies C and D appear to merge with the Nazca slab anomaly (Fig. 11, lines C–C′ and D–D′) due to the vertical smearing even though the input

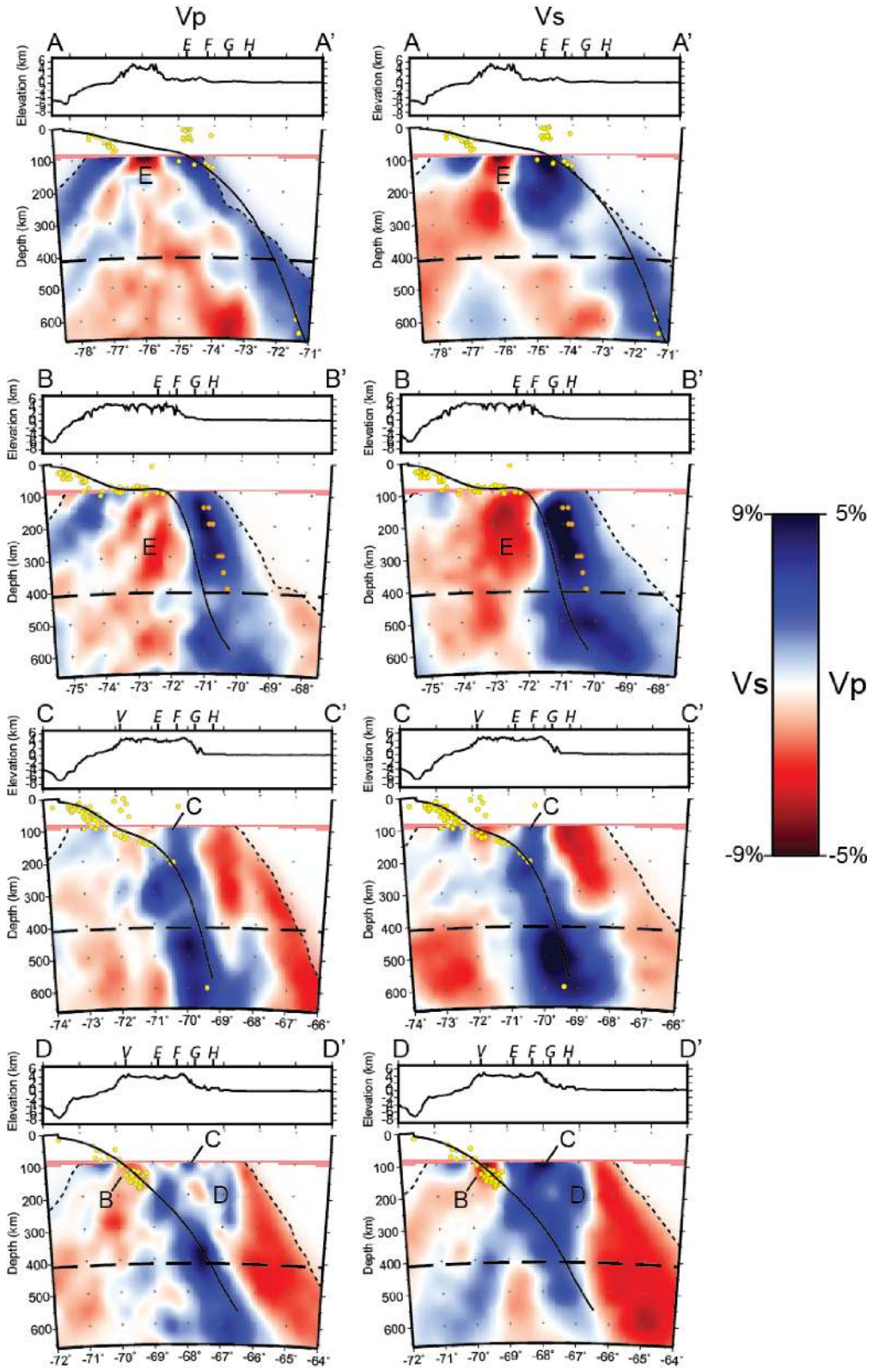

Figure 9. Trench perpendicular cross-sections through the tomography model for both Vp (left) and Vs (right). Cross-section locations are as shown in Fig. 1. Dashed lines are the same as in Fig. 6. Location of active volcanic arc marked with a V. Intersection with trench parallel cross-sections indicated by italicized letters E, F, G and H. Yellow dots are earthquake locations from the EHB catalogue (Engdahl *et al.* 1998). Solid black line marks the top of the Nazca slab from the Slab1.0 model (Hayes *et al.* 2012). Orange dots mark reflection points from James & Snoke (1990). Labelled anomalies (B, C, D and E) are discussed in the text.

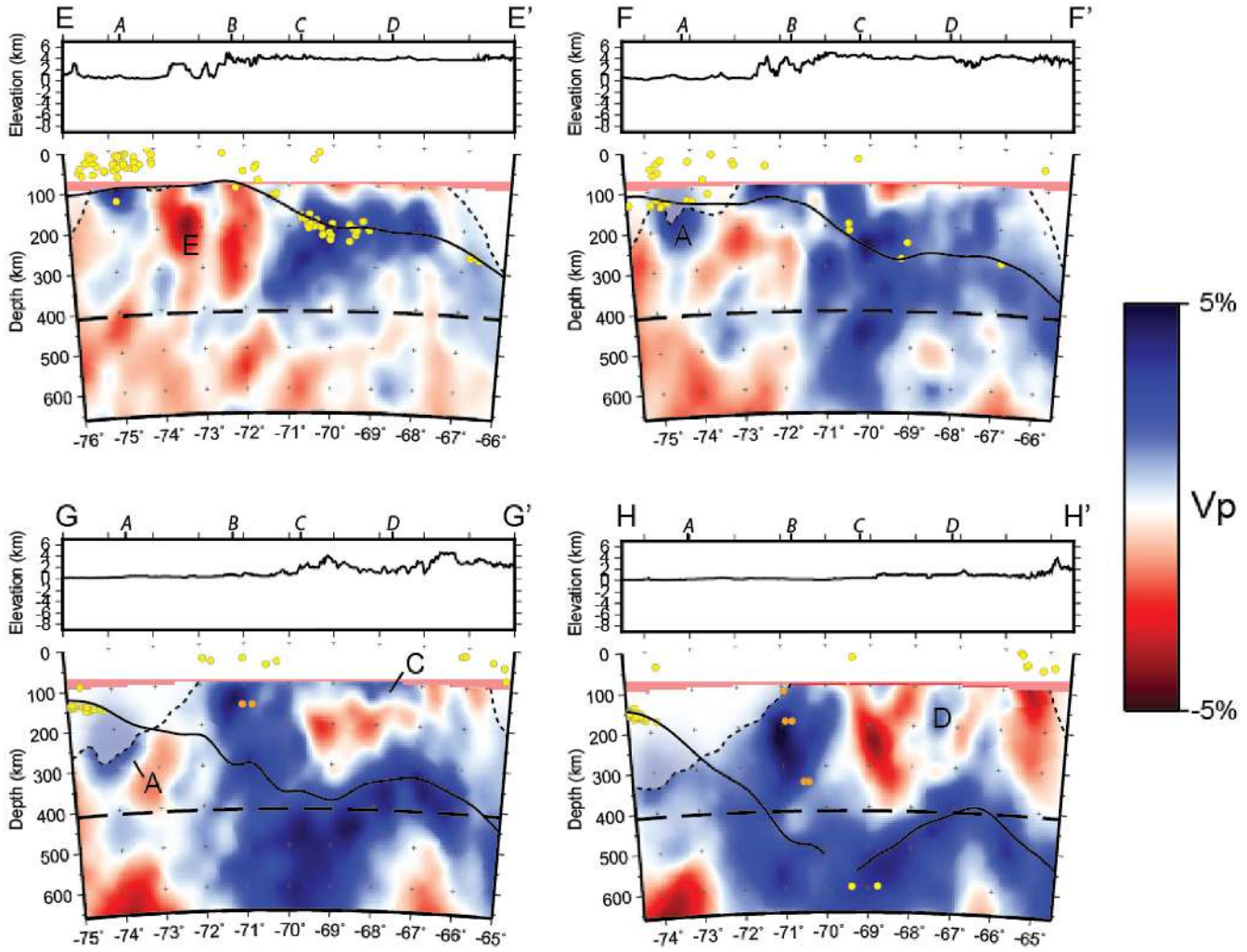

Figure 10. Trench parallel cross-sections through the Vp tomography model. Cross-section locations are as shown in Fig. 1. Dashed lines are the same as in Fig. 6. Intersection with trench perpendicular cross-sections indicated by italicized letters A, B, C and D. Yellow dots are earthquake locations from the EHB catalogue (Engdahl *et al.* 1998). Solid black line marks the top of the Nazca slab from the Slab1.0 model (Hayes *et al.* 2012). Orange dots mark reflection points from James & Snoke (1990). Labelled anomalies (A, C, D and E) are discussed in the text. Cross-sections through the Vs tomography model are shown in the Supporting Information Fig. S11.

anomalies are clearly separate. We conclude that these anomalies are real even if there is some uncertainty about the depth extent of the anomalies.

High-amplitude low-velocity anomalies in the *S*-wave tomograms (−5 to −6 per cent) are seen in the MTZ between 410 and 660 km depth above the subducting Nazca slab at the eastern edge of the study area with some continuation of the low-velocity anomaly into the upper mantle above 410 km depth (Figs 8 and 9). Similar low-velocity anomalies are seen in the *P*-wave tomograms above the slab in the MTZ. However, the resolution of this anomaly is complicated by artefacts of the inversion as seen in Fig. 4 and therefore additional data is required to constrain the extent and amplitude of this anomaly before we can offer an interpretation of its origin.

The sub-slab mantle

The shallow mantle in the northern part of our study region is dominated by high-amplitude slow anomalies in the mantle below the Peruvian flat slab (Anomaly E, Figs 6, 7, 9 and 10). This high-amplitude slow anomaly extends vertically through several depth slices. The southern part of the low-velocity anomaly, Anomaly E, appears to be confined to the area under the projection of the Nazca Ridge and extends from 95 to ∼400 km depth. The high-amplitude slow velocity anomaly continues to the north but is confined to the uppermost depth slices, 95 km and 130 km. Synthetic recovery tests (Line A–A′, Fig. 11) indicates that we can resolve Anomaly E in the depth range of 130–400 km but not the shallow portion. Anomaly E in the north is limited to the shallow depth range where we have limited resolution in our recovery test, therefore we are hesitant to interpret the northern extent of the anomaly since it could be complicated by vertical smearing of shallower anomalies. The eastern edge of our resolution does not extend past the region where the Nazca slab begins to subduct steeply into the mantle inboard of the Peruvian flat slab so no observations of the mantle above the slab can be made. There is also a high-amplitude low-velocity region in the MTZ below the slab in the *S*-wave model (Fig. 11, C–C′). This anomaly is less prominent in the *P*-wave model, hence we are not interpreting it.

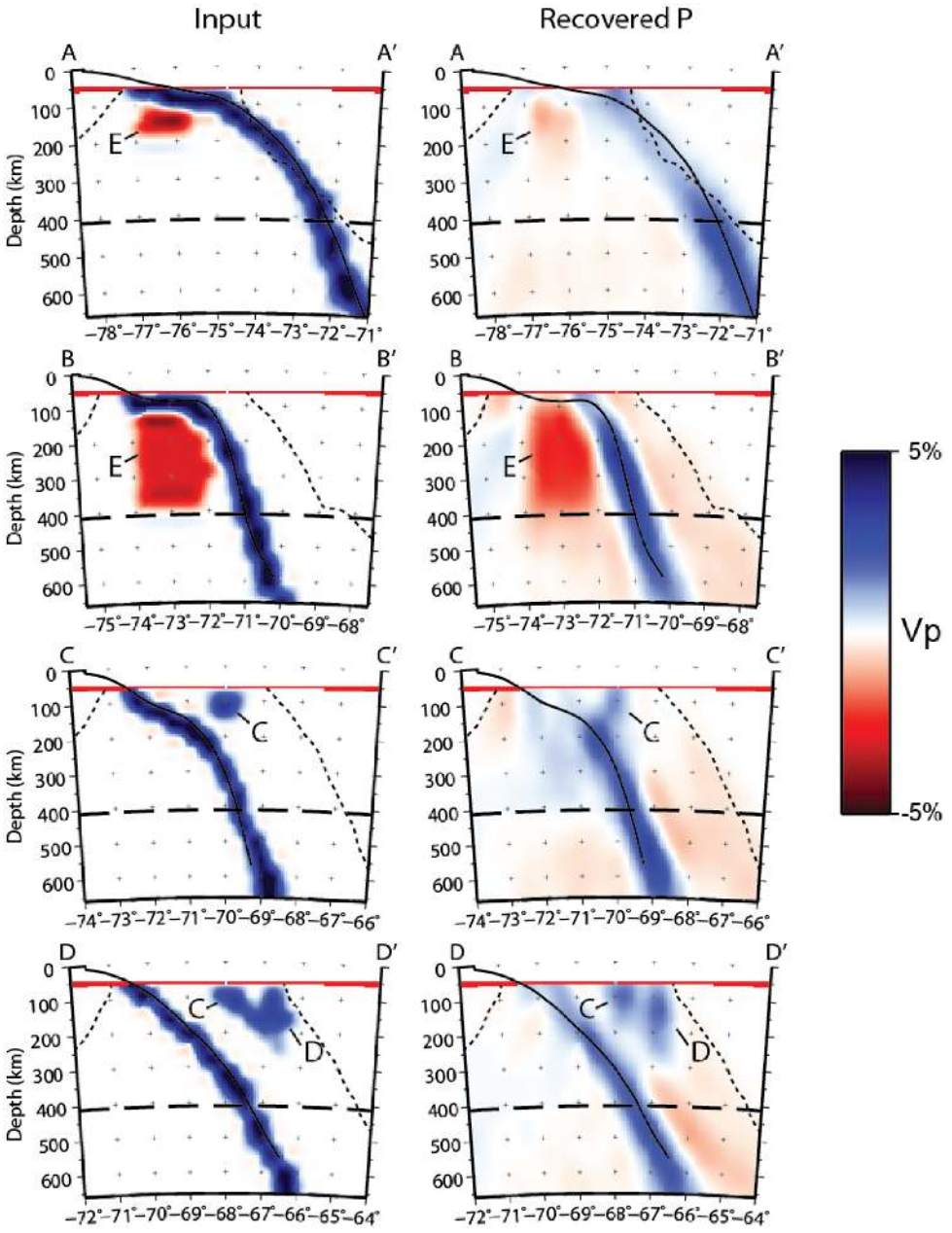

Figure 11. Cross-section results for our synthetic anomaly recovery tests for *P*-wave inversion. Cross-section locations are shown in Fig. 1. Dashed lines are the same as in Fig. 6. The geometry of our input slab model is based on the Slab1.0 contours (black line, Hayes *et al.* 2012). Labelled anomalies (C, D and E) based on output from tomographic inversion. Synthetic input (left) and recovered Vp (right) models are shown. Decreased amplitude recovery and vertical smearing of the recovered slab anomaly is observed in the upper 200 km of the model. In general, the amplitude recovery increases with depth. Cross-sections through the synthetic anomaly tests for the *S*-wave inversion and depth slices for both the *P*- and *S*-wave inversions are shown in the Supporting Information Figs S6–S8.

DISCUSSION

Geometry of the subducting Nazca slab

The fast slab anomaly that we image in our tomograms allows us to make some observations about the geometry of the Nazca slab. We use our results to offer some modifications to the Slab1.0 global subduction zone model, which is primarily constrained by slab seismicity in our study region (Hayes *et al.* 2012). The slab contours in Fig. 12 were determined by tracing the centre of the fast slab anomaly in the *P*-wave tomograms associated with the subducting slab at depths below 200 km on the depth slices. The centre of the anomaly was chosen due to the limited ability of tomography to resolve discontinuities, making it difficult to constrain the top of the slab solely using our results. Therefore the centre of the slab anomaly represents the best estimate of the location of the slab from our tomography. The location of the subducting slab above 200 km is constrained using a combination of our results, the location of intermediate depth seismicity from the EHB catalogue (Engdahl *et al.* 1998), the Slab1.0 global subduction zone model (Hayes *et al.* 2012) and initial constraints on the location of the top of the Peruvian flat slab north of 14°S from receiver function work by Bishop *et al.* (2013). Relocated earthquakes from Schneider &

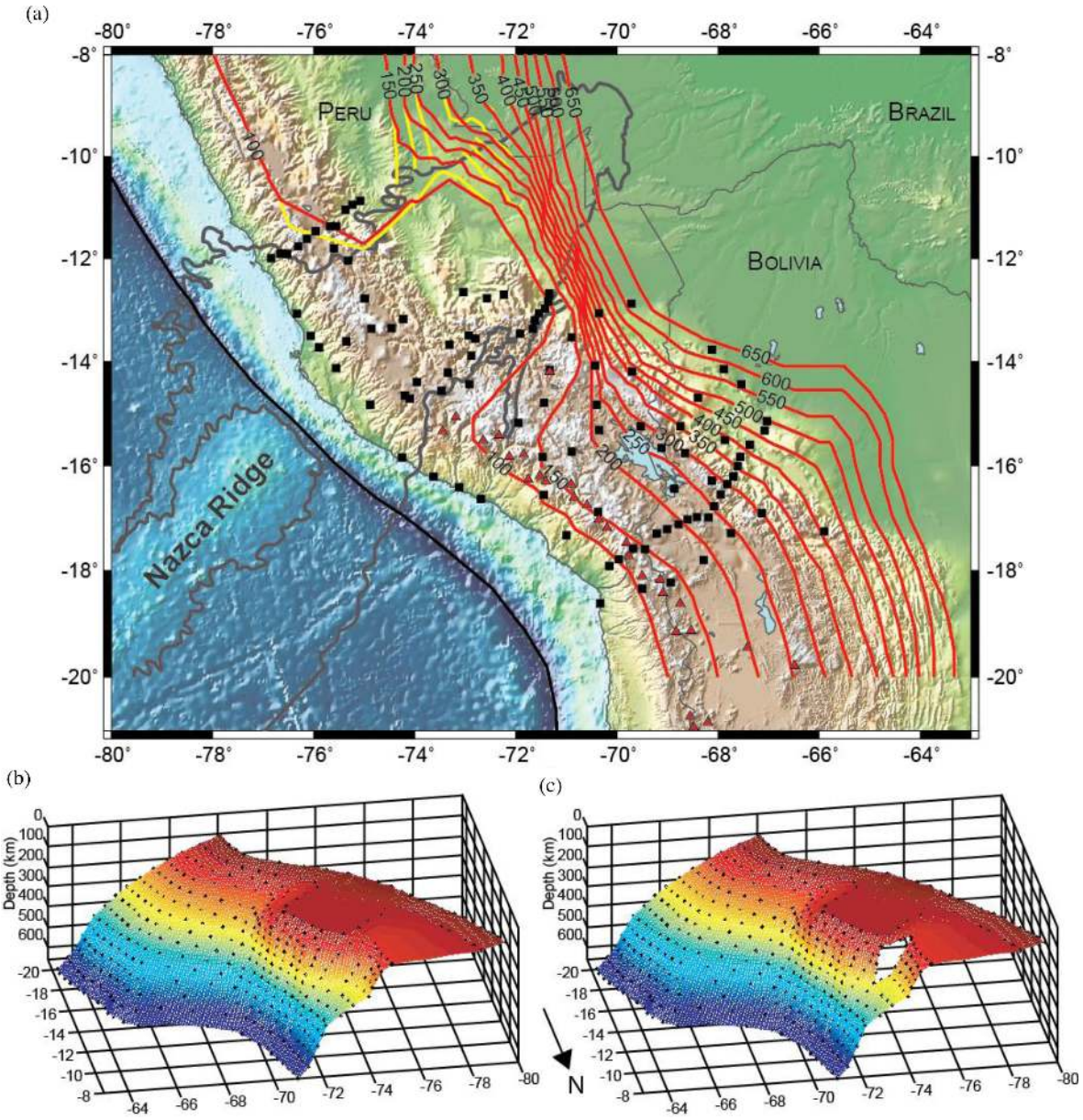

Figure 12. (a) Slab contours determined from this study. Red contours are continuous slab contours determined using constraints discussed in the text (Supporting Information Table S1). Yellow contours are disrupted by the hypothesized tear north of the Nazca Ridge. Red triangles mark location of Holocene volcanoes (Siebert & Simkin 2002). Grey outline marks the projection of the subducted Nazca Ridge from Hampel (2002). Solid black line to the west of the coast marks the location of the Peru–Chile trench. (b) 3-D mesh of continuous slab contours without hypothesized tear. Note that north is towards the bottom of the figure for 3-D mesh surfaces. Mesh surface and slab contours were created by using a linear interpolation between data points from our results (black dots). (c) 3-D mesh of slab contours with hypothesized tear on the north side of the Nazca Ridge.

Sacks (1987) are used to define the geometry and location of the change in slab dip from 100 to 200 km depth just to the south of the Nazca Ridge between 14° and 16°S. A linear interpolation between the points from our results is then used to create a continuous slab surface, allowing us to calculate slab contours at even depth intervals (Fig. 12).

Transitioning from flat to normal subduction and the effect of the Nazca Ridge

Intermediate depth seismicity marks the region where the slab dip changes from shallow subduction along the subducted Nazca Ridge to normal subduction under Bolivia to the south. Although this bend in the slab is not resolved at 95 or 130 km depths, probably due to interference from high-amplitude low-velocity anomalies at these depths, slab earthquakes mark the location of the slab at these depths. When combined with the location of the steepening slab inboard of the Nazca Ridge, these results indicate that the transition from shallow to normal subduction is marked by rapid bending of the slab in the shallow mantle directly south of the ridge. Seismicity from the EHB catalogue (Fig. 6; Engdahl *et al.* 1998) combined with work by Schneider & Sacks (1987) allows us to constrain the location of the subducting slab at 95, 130 and 165 km depth near 14°S and are taken into account in the slab contours in Fig. 12. At depths greater than 200 km, the slab is imaged as a continuous

fast anomaly, which bends in the mantle between the shallowly subducting Nazca Ridge and the normally subducting slab to the south.

At the northern edge of our study region, near 10°, the high-amplitude fast anomaly (Anomaly A; Figs 6 and 10) appears to correspond to intraslab earthquakes at 130 and 165 km depth; we interpret this anomaly as the Nazca slab. This anomaly is offset by ∼100 km from the observed slab anomaly under the projection of the Nazca Ridge indicating that the slab has either undergone abrupt bending just north of the subducted Nazca Ridge or a small, ridge parallel tear in the slab exists along the north edge of the Nazca Ridge (Fig. 12). Although we are unable to directly image the slab in the region where the postulated tear exists, the lack of intermediate depth seismicity there combined with the offset in the slab anomaly leads us to conclude that a tear is possible on the north side of the ridge, unlike at its southern edge where bending in the slab is marked by a limited region of intermediate depth seismicity. The offset in the slab anomaly north of the subducting Nazca Ridge decreases with depth until 365 km where a continuous slab anomaly is imaged, leading us to conclude that the vertical extent of any possible tear is limited to between 130 and 365 km depth (Fig. 12). The amount of offset of the slab lithosphere by the hypothesized tear is uncertain due to our limited resolution in the area and therefore we are unable to determine if sufficient offset exists to allow for flow of subslab mantle material through the tear. Since we cannot directly image the region along the north side of the Nazca Ridge due to limitations in our resolution, confirmation of the existence of the hypothesized tear will require future work in the area. Due to the uncertainty in our interpretation, we offer a set of slab contours that assume that the slab north of the Nazca Ridge is continuous (Fig. 12, Supporting Information Table S1).

Along the subducted projection of the Nazca Ridge (north of 14°S) the slab anomaly between 165 km depth and the top of the MTZ, 410 km depth, appears to be further inland than is indicated by the Slab1.0 global subduction zone model contours (Fig 1b; Hayes *et al.* 2012). This indicates that the Peruvian flat slab extends further inland than was previously thought along the projection of the Nazca Ridge (Figs 7–9). Since the slab inboard of the subducting Nazca Ridge is aseismic (Fig. 1b) and limited geophysical work has been done previously in this area, this segment of the Nazca slab is not well-constrained in the Slab1.0 global subduction zone model. Our results are in agreement with work by James & Snoke (1990), who used underside wide-angle reflections from the upper surface of the mostly aseismic part of the Nazca slab in this area to locate the top of the slab (Figs 6–10). This indicates that the dip of the Nazca slab once it re-steepens inboard of the flat slab region is very steep (between 70° and 75°) below depths of about 150 to 200 km. This region of slab steepening corresponds to the southeast edge of the projection of the subducted Nazca Ridge based on the conjugate feature, the Tuamotu Plateau (Fig. 7; Hampel 2002), implying that the presence of the ridge is locally influencing the geometry of the flat slab.

Although the shallow depth of Anomaly E is not very well resolved we still speculate on the implication that there are low velocities at the base of the Nazca plate under the Nazca Ridge. The low-velocity anomaly under the southern Peruvian flat slab (shallow part of Anomaly E, Figs 6, 7, 9 and 10) could be associated in part with the presence of relatively hot, asthenospheric mantle at anomalously shallow depths due to the existence of thinned oceanic mantle lithosphere under the Nazca Ridge. A region of decreased elastic thickness associated with the Nazca Ridge has been proposed by Tassara *et al.* (2007), who suggest that it is related to weakening of the oceanic lithosphere due to interactions with known hotspots. Anomalously thin oceanic mantle lithosphere is also observed in association with the Hawaiian hotspot (Li *et al.* 2004) leading us to conclude that similar thinning of the oceanic mantle lithosphere under the Nazca Ridge is possible. Dating of some of the lavas that make up the Nazca Ridge indicates that much of the ridge is between 5 and 13 Myr younger than the seafloor onto which the ridge was emplaced (Ray *et al.* 2012). This implies that lithospheric cooling of the Nazca plate could have been disrupted by the Easter-Salas hotspot, which was located to the east of the axis of the East Pacific Rise during at least some of the formation of the Nazca Ridge, leading to a thinner lithosphere under the Nazca Ridge than expected considering the ∼45 Ma age of the oceanic plate (Müller *et al.* 2008).

Anomaly E extends to a depths of nearly ∼400 km so it is unlikely that the entire anomaly is due to the formation of the Nazca Ridge. However, the overall spatial correlation with the subducting Nazca Ridge, and the very steep portion of the deeper slab, is intriguing. We speculate that the deeper portion of Anomaly E (above the MTZ) may be related to upward flow from the MTZ adjacent to the steep and thickened segment of the subducting Nazca Plate (Hirschmann 2006).

Variations in the central Andean shallow mantle (95–200 km)

Between 95 and 130 km depth, we observe slow velocities under the western Altiplano in the southern part of our study area (Anomaly B, Figs 6 and 9) and a fast, variable anomaly under the Eastern Cordillera and Subandean Zone (Anomaly C, Figs 6 and 9). The low-velocity anomaly, Anomaly B, is particularly prominent in the *S*-wave inversion and interferes with our ability to resolve a continuous, steeply dipping Nazca slab anomaly under Bolivia. This anomaly is consistent with the presence of a region of partial melting of the mantle above the subducting Nazca slab, which serves as the source region for the arc volcanism observed in the Western Cordillera. The higher amplitude of this anomaly in the *S*-wave tomograms in comparison to the *P*-wave tomograms is consistent with the presence of melt, which more strongly affects *S*-wave velocities (Nakajima *et al.* 2001). Similar anomalies associated with arc source regions have been seen elsewhere in the Andes in both teleseismic (e.g. Heit *et al.* 2008) and local (e.g. Schurr *et al.* 2006) tomography studies.

The fast anomaly (Anomaly C) that we observe under the Eastern Cordillera and Subandean Zone between 14° and 18° S in both the *P*- and *S*-wave inversions is bounded to the northeast by a well-resolved low-velocity anomaly (Fig. 6). Although other studies in the central Andes (e.g. Dorbath *et al.* 1993; Myers *et al.* 1998; Beck & Zandt 2002; Phillips *et al.* 2012; Scire *et al.* 2015) have postulated underthrusting of Brazilian cratonic lithosphere as far west as the Eastern Cordillera, the presence of the low-velocity anomaly inboard of Anomaly C suggests that this fast anomaly is unlikely to represent undisrupted cratonic lithosphere. As a possible alternative to underthrusting of Brazilian cratonic lithosphere, Scire *et al.* (2015) proposed that a similar elongated fast anomaly under the Eastern Cordillera between 16° and 25°S could be related to foundering of cold lithospheric material. This interpretation implies that lithospheric material is being removed along much of the eastern edge of the Andes. The vertically elongated fast anomaly, which descends from 95 to 200 km depth near 15°S under the Subandean Zone (Anomaly D; Figs 6, 7, 9 and 10), is similar to

anomalies that have been observed in other parts of the Andes, particularly under the Puna Plateau to the south. Previous studies have interpreted these anomalies as delaminating blocks of lithosphere (e.g. Koulakov *et al.* 2006; Schurr *et al.* 2006; Bianchi *et al.* 2013; Beck *et al.* 2015; Scire *et al.* 2015). The presence of anomalously slow velocities at depths below 95 km in the mantle adjacent to Anomaly D could be indicative of upwelling asthenosphere resulting from piecemeal delamination of the mantle lithosphere. Similar low velocities in the shallow mantle have been interpreted as asthenospheric mantle at shallow depths under the central Andes (e.g. Myers *et al.* 1998; Heit *et al.* 2008). Since our resolution is limited to depths below 95 km, we are unable to image the top of the hypothesized delaminating block or where it is connected to the Andean crust if such a connection exists. Therefore we are limited in our ability to interpret the timing of the hypothesized delamination event and its possible effects on the crust; future studies using methods with better resolution in the shallow mantle and crust should clarify the interpretation.

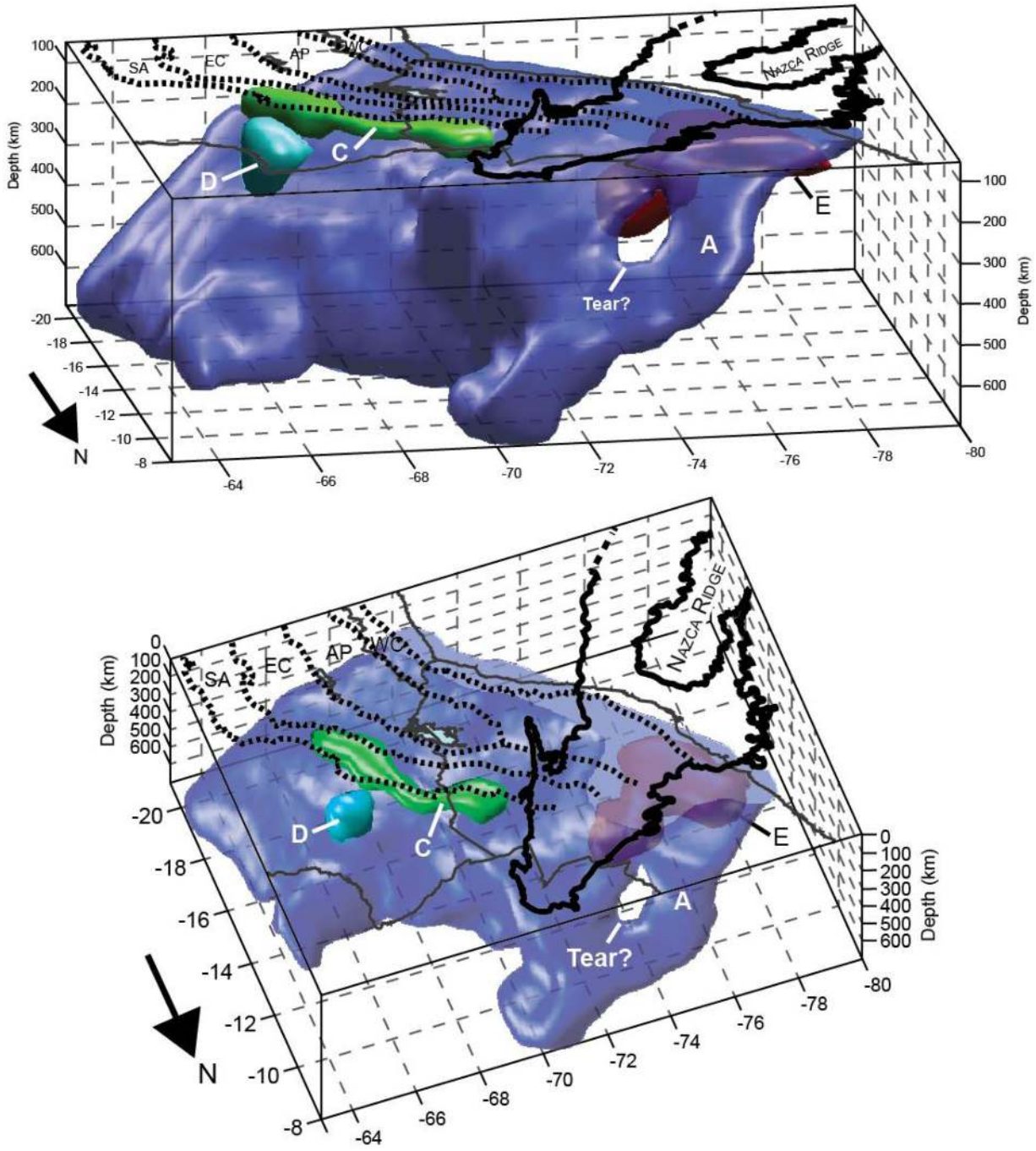

Figure 13. 3-D diagram of the resolved subducting Nazca slab and prominent mantle low-velocity anomalies inferred from our tomographic models. The isosurfaces for this diagram are obtained by tracing the most coherent low-velocity anomalies (less than negative 3 per cent) and slab-related (greater than positive 3 per cent) coherent fast anomalies in the tomographic model. Geomorphic provinces (fine dashed lines) are the same as in Fig. 1(a). Heavy black outline marks the projection of the subducted Nazca Ridge from Hampel (2002). Anomalies A, C, D and E labelled as in previous figures.

Deformation of the slab in the MTZ

As previously discussed, the slab anomaly is easily identified and appears to be continuous below 200 km depth although it is further inland in the northern part of our study region than indicated by the Slab1.0 global subduction zone contours (Figs 7 and 8). A cluster of deep earthquakes (∼600 km depth) is observed in the northern part of our study region. Additional isolated deep earthquakes occur between 500 and 600 km depth to the south of the large cluster. The location of those earthquakes falls within our fast slab anomaly, in agreement with the idea that deep focus earthquakes occur within the cold cores of slab in the MTZ (e.g. Green & Houston 1995; Kirby *et al.* 1996; Wiens 2001). In the region where we have resolution northeast of the slab anomaly between 8° and 14°S, we do not see any evidence that the Nazca slab has stagnated for any significant distance to the east in the MTZ. This agrees with global tomography studies which observe a diffuse fast anomaly in the lower mantle that corresponds with the location of the subducting Nazca slab and indicates that the Nazca slab does not experience long-term stagnation in the MTZ and instead continues subducting into the lower mantle (e.g. Bijwaard *et al.* 1998; Fukao *et al.* 2001; Zhao 2004; Li *et al.* 2008, 2009; Zhao *et al.* 2013). Our results do show a region of localized widening of the Nazca slab anomaly in the MTZ between 8° and 14°S, similar to observations made further south (Scire *et al.* 2015). Thickening of slab anomalies in the MTZ has been observed in global tomography studies and has been interpreted as evidence of temporary stagnation in the MTZ. This results in either thickening of the slab before subduction resumes into the lower mantle (e.g. Bijwaard *et al.* 1998; Li *et al.* 2008) or folding of the slab to accommodate a decreasing sinking velocity in the lower mantle (e.g. Ribe *et al.* 2007). The location of this region of thickening corresponds to the very steep (∼70°) dip of subduction due to the effect of the Peruvian flat slab on the inboard location of the Nazca slab and is possibly influenced by the Nazca slab intersecting the base of the MTZ at a near vertical angle. Between 14° and 17°S, the Nazca slab anomaly bends and thins in the MTZ. This is particularly apparent in the *P*-wave tomography, where the slab anomaly changes strike from almost due east to a north-south orientation in the lower MTZ (Fig. 8). This change in strike of the slab in the MTZ corresponds to the location of the Bolivian orocline and possibly represents the translation of the orocline from the surface down to MTZ depths.

CONCLUSION

Our teleseismic tomography study shows new *P*- and *S*-wave tomograms of the subducting Nazca slab down to the base of the MTZ, including the transition from shallow, flat slab subduction in the north to more normally dipping subduction in the south (Fig. 13). We propose new slab contours for the Nazca slab between 8° and 20°S from 100 to 660 km depth based on a combination of our results below ∼200 km and work in the region by other studies for the region above ∼200 km (Fig. 12; Supporting Information Table S1). We tentatively suggest a possible slab tear along the north side of the Nazca Ridge at 10°S between 71° and 73°W (Fig. 12) although due to limitations of our resolution to the north of the Nazca Ridge, confirmation of the existence of this tear will rely on future work. We observe a high-amplitude low-velocity anomaly under the Nazca Ridge (Anomaly E, Fig. 13) that may be in part due to thinned oceanic mantle lithosphere and upward flow from the MTZ. Our results show a vertically elongated fast anomaly under the Subandean Zone between 95 and 200 km depth (Anomaly D, Fig. 13). Considering both the elongated vertical geometry of the fast anomaly and the adjacent low-velocity anomalies in both the *P*- and *S*-wave models, we propose that this corresponds to a block of delaminating lithosphere. North of 14°S, we image the Nazca slab to the east of its predicted location from the Slab1.0 global subduction zone model where it steepens inboard of the Peruvian flat slab region. This indicates that the slab remains flat further inland than was previously thought, and that when it steepens and resumes subduction into the mantle, it does so at a very steep (∼70°) angle. This region of slab steepening corresponds with the predicted edge of the subducted Nazca Ridge (Hampel 2002), implying that the geometry of the Nazca slab is at least locally being influenced by the presence of the ridge. When this very steeply dipping slab hits the 660 km discontinuity at the base of the MTZ, we observe local thickening of the Nazca slab between 8° and 14°S, consistent with temporary stagnation of the slab in the MTZ before it resumes subduction into the lower mantle. Further south, in the normally dipping subduction zone, the slab shows less thickening in the MTZ.

ACKNOWLEDGEMENTS

Support for this research was provided by the National Science Foundation as part of the CAUGHT (NSF Award EAR-0907880) and PULSE (NSF Award EAR-0943991) projects. The seismic instruments for the CAUGHT and PULSE arrays were provided by the Incorporated Research Institutions for Seismology (IRIS) through the PASSCAL Instrument Center at New Mexico Tech, Yale University and the University of North Carolina, Chapel Hill. Data collected are or will be available through the IRIS Data Management Center. The facilities of the IRIS Consortium are supported by the National Science Foundation under Cooperative Agreement EAR-1063471, the NSF Office of Polar Programs and the DOE National Nuclear Security Administration. The Global Seismographic Network (GSN) is a cooperative scientific facility operated jointly by the Incorporated Research Institutions for Seismology (IRIS), the United States Geological Survey (USGS) and the National Science Foundation (NSF). The authors would like to acknowledge the GEOFON Program at GFZ Potsdam as a source of additional waveform data. We thank Rob Clayton and Paul Davis for providing PeruSE data. The authors thank Brandon Schmandt at the University of New Mexico and Gene Humphreys at the University of Oregon as the original authors of the teleseismic tomography code used in this study. Chevron, ConocoPhillips and ExxonMobil provided additional support for Alissa Scire.

REFERENCES

Anderson, M., Zandt, G., Triep, E., Fouch, M. & Beck, S., 2004. Anisotropy and mantle flow in the Chile–Argentina subduction zone from shear wave splitting analysis, *Geophys. Res. Lett.,* **31,** L23608, doi:10.1029/2004GL020906.

Asch, G. *et al.*, 2006. Seismological studies of the central and southern Andes, in *The Andes—Active Subduction Orogeny*, pp. 443–457, eds Oncken, O., Chong, G., Franz, G., Giese, P., Götze, H.-J., Ramos, V.A., Strecker, M.R. & Wigger, P., Springer-Verlag.

Barazangi, M. & Isacks, B.L., 1976. Spatial distribution of earthquakes and subduction of the Nazca plate beneath South America, *Geology,* **4,** 686–692.

Barazangi, M. & Isacks, B.L., 1979. Subduction of the Nazca plate beneath Peru: evidence from spatial distribution of earthquakes, *Geophys. J. R. astr. Soc.,* **57,** 537–555.

Beck, S.L. & Zandt, G., 2002. The nature of orogenic crust in the central Andes, *J. Geophys. Res.,* **107,** 2230–2247.

Beck, S.L., Zandt, G. & Wagner, L., 2010. Central Andean Uplift and the Geodynamics of High Topography, Other/Seismic Network, International Federation of Digital Seismograph Networks, doi:10.7914/SN/ZG_2010.

Beck, S.L., Zandt, G., Ward, K.M. & Scire, A., 2015. Multiple styles and scales of lithospheric foundering beneath the Puna Plateau, Central Andes, in *Geodynamics of a Cordilleran Orogenic System: The Central Andes of Argentina and Northern Chile*, pp. 43–60, eds DeCelles, P.G., Ducea, M.N., Carrapa, B. & Kapp, P., Geological Society of America Memoir **212**.

Bianchi, M. *et al.*, 2013. Teleseismic tomography of the southern Puna plateau in Argentina and adjacent regions, *Tectonophysics,* **586,** 65–83.

Bijwaard, H., Spakman, W. & Engdahl, E.R., 1998. Closing the gap between regional and global travel time tomography, *J. Geophys. Res.,* **103,** 30 055–30 078.

Biryol, C.B., Beck, S.L., Zandt, G. & Özacar, A.A., 2011. Segmented African lithosphere beneath the Anatolian region inferred from teleseismic *P*-wave tomography, *Geophys. J. Int.,* **184,** 1037–1057.

Bishop, B., Beck, S.L., Zandt, G., Kumar, A., Wagner, L.S., Long, M.D. & Tavera, H., 2013. Receiver Function Study of the Peruvian Flat-Slab Region: initial results from PULSE, in *Proceedings of the AGU Fall Meeting*, San Francisco, CA, Abstract T33B–2632.

Boyd, T.M., Snoke, J.A., Sacks, I.S. & Rodriguez, A.B., 1984. High-resolution determination of the Benioff zone geometry beneath southern Peru, *Bull. seism. Soc. Am.,* **74,** 559–568.

Burd, A.I., Booker, J.R., Mackie, R., Pomposiello, C. & Favetto, A., 2013. Electrical conductivity of the Pampean shallow subduction region of Argentina near 33 S: evidence for a slab window, *Geochem. Geophys. Geosyst.,* **14**(8), 3192–3209.

Cahill, T. & Isacks, B.L., 1992. Seismicity and shape of the subducted Nazca plate, *J. Geophys. Res.,* **97,** 17 503–17 529.

Dahlen, F.A., Hung, S.-H. & Nolet, G., 2000. Fréchet kernels for finite-frequency traveltimes - 1. Theory, *Geophys. J. Int.,* **141,** 157–174.

Dorbath, C. & Granet, M., 1996. Local earthquake tomography of the Altiplano and the Eastern Cordillera of northern Bolivia, *Tectonophysics,* **259,** 117–136.

Dorbath, C. & Masson, F., 2000. Composition of the crust and upper-mantle in the Central Andes (19°30'S) inferred from *P* wave velocity and Poisson's ratio, *Tectonophysics,* **327,** 213–223.

Dorbath, C., Granet, M., Poupinet, G. & Martinez, C., 1993. A teleseismic study of the Altiplano and the Eastern Cordillera in Northern Bolivia: new constraints on a lithospheric model, *J. Geophys. Res.,* **98,** 9825–9844.

Dorbath, L., Dorbath, C., Jimenez, E. & Rivera, L., 1991. Seismicity and tectonic deformation in the Eastern Cordillera and the sub-Andean zone of central Peru, *J. South Am. Earth Sci.,* **4,** 13–24.

Dougherty, S.L. & Clayton, R.W., 2015. Seismic structure in southern Peru: evidence for a smooth contortion between flat and normal subduction of the Nazca Plate, *Geophys. J. Int.,* **200,** 534–555.

Eakin, C.M. & Long, M.D., 2013. Complex anisotropy beneath the Peruvian flat slab from frequency-dependent, multiple-phase shear wave splitting analysis, *J. Geophys. Res.,* **118,** 4794–4813.

Eakin, C.M., Long, M.D., Beck, S.L., Wagner, L.S., Tavera, H. & Condori, C., 2014. Response of the mantle to flat slab evolution: insights from local S splitting beneath Peru, *Geophys. Res. Lett.,* **41,** 3438–3446.

Elger, K., Oncken, O. & Glodny, J., 2005. Plateau-style accumulation of deformation: Southern Altiplano, *Tectonics,* **24,** TC4020, doi:10.1029/2004TC001675.

Engdahl, E.R., van der Hilst, R.D. & Berrocal, J., 1995. Imaging of subducted lithosphere beneath South America, *Geophys. Res. Lett.,* **22,** 2317–2320.

Engdahl, E.R., van der Hilst, R.D. & Buland, R., 1998. Global teleseismic earthquake relocation with improved travel times and procedures for depth determination, *Bull. seism. Soc. Am.,* **88,** 722–743.

Espurt, N., Funiciello, F., Martinod, J., Guillaume, B., Regard, V., Faccenna, C. & Brusset, S., 2008. Flat slab subduction dynamics and deformation of the South American plate: insights from analog modeling, *Tectonics,* **27,** TC3011, doi:10.1029/2007TC002175.

Fukao, Y., Widiyantoro, S. & Obayashi, M., 2001. Stagnant slabs in the upper and lower mantle transition region, *Rev. Geophys.,* **39,** 291–323.

Fukao, Y., Obayashi, M., Nakakuki, T. & the Deep Slab Project Group, 2009. Stagnant slab: a review, *Annu. Rev. Earth Planet. Sci.,* **37,** 19–46.

Gans, C.R., Beck, S.L., Zandt, G., Gilbert, H., Alvarado, P., Anderson, M. & Linkimer, L., 2011. Continental and oceanic crustal structure of the Pampean flat slab region, western Argentina, using receiver function analysis: new high resolution results, *Geophys. J. Int.,* **186**(1), 45–58.

Garzione, C., Hoke, G., Libarkin, J., Withers, S., McFadden, B., Eiler, J., Ghosh, P. & Mulch, A., 2008. Rise of the Andes, *Science,* **320,** 1304–1307.

Gerya, T.V., Fossati, D., Cantieni, C. & Seward, D., 2009. Dynamic effects of aseismic ridge subduction: numerical modeling, *Eur. J. Mineral.,* **21**(3), 649–661.

Ghosh, P., Garzione, C. & Eiler, J., 2006. Rapid uplift of the Altiplano revealed through 13C-18O bonds in paleosol carbonates, *Science,* **311,** 511–515.

Graeber, F.M. & Asch, G., 1999. Three-dimensional models of *P* wave velocity and P-to-S velocity ratio in the southern central Andes by simultaneous inversion of local earthquake data, *J. Geophys. Res.,* **104,** 20 237–20 256.

Green, H.W. & Houston, H., 1995. The mechanics of deep earthquakes, *Annu. Rev. Earth Planet. Sci.,* **23,** 169–213.

Gutscher, M.-A., 2002. Andean subduction styles and their effect on thermal structure and interpolate coupling, *J. South Am. Earth Sci.,* **15,** 3–10.

Gutscher, M.-A., Malavieille, J., Lallemand, S. & Collot, J.-Y., 1999a. Tectonic segmentation of the North Andean margin: impact of the Carnegie Ridge collision, *Earth planet. Sci. Lett.,* **68,** 255–270.

Gutscher, M.-A., Olivet, J.-L., Aslanian, D., Eissen, J.-P. & Maury, R., 1999b. The "lost Inca Plateau": cause of flat subduction beneath Peru?, *Earth planet. Sci. Lett.,* **171,** 335–241.

Gutscher, M.-A., Spakman, W., Bijwaard, H. & Engdahl, E.R., 2000. Geodynamics of flat subduction: seismicity and tomographic constraints from the Andean margin, *Tectonics,* **19,** 814–833.

Hampel, A., 2002. The migration history of the Nazca Ridge along the Peruvian active margin: a re-evaluation, *Earth planet. Sci. Lett.,* **203,** 665–679.

Hampel, A., Kukowski, N., Bialas, J., Huebscher, C. & Heinbockel, R., 2004. Ridge subduction at an erosive margin: the collision zone of the Nazca Ridge in southern Peru, *J. Geophys. Res.,* **109,** B02101, doi:10.1029/2003JB002593.

Hasegawa, A. & Sacks, I.S., 1981. Subduction of the Nazca Plate beneath Peru as determined from seismic observations, *J. Geophys. Res.,* **86,** 4971–4980.

Hayes, G.P., Wald, D.J. & Johnson, R.J., 2012. Slab1.0: a three-dimensional model of global subduction zone geometries, *J. Geophys. Res.,* **117,** B01302, doi:10.1029/2011JB008524.

Heit, B., Koulakov, I., Asch, G., Yuan, X., Kind, R., Alcocer-Rodriguez, I., Tawackoli, S. & Wilke, H., 2008. More constraints to determine the seismic structure beneath the Central Andes at 21°S using teleseismic tomography analysis, *J. South Am. Earth Sci.,* **25,** 22–36.

Hirschmann, M.M., 2006. Water, melting and the deep Earth H_2O cycle, *Annu. Rev. Earth Planet. Sci.,* **34,** 629–653.

Hung, S.-H., Dahlen, F.A. & Nolet, G., 2000. Fréchet kernels for finite-frequency traveltimes–II. Examples, *Geophys. J. Int.,* **141,** 175–203.

Isacks, B.L., 1988. Uplift of the Central Andean Plateau and bending of the Bolivian orocline, *J. Geophys. Res.,* **93,** 3211–3231.

Isacks, B. & Barazangi, M., 1977. Geometry of Benioff zones: Lateral segmentation and downwards bending of the subducted lithosphere, in *Island Arcs, Deep Sea Trenches and Back Arc Basins*, pp. 99–114, eds Talwani, M. & Pitman, W., American Geophysical Union, Ewing Series 1.

James, D.E. & Snoke, J.A., 1990. Seismic evidence for continuity of the deep slab beneath central and eastern Peru, *J. Geophys. Res.,* **85,** 4989–5001.

Kay, R.W. & Kay, S.M., 1993. Delamination and delamination magmatism, *Tectonophysics,* **219,** 177–189.

Kay, S.M. & Coira, B., 2009. Shallowing and steepening subduction zones, continental lithosphere loss, magmatism and crustal flow under the Central Andean Altiplano-Puna Plateau, in *Backbone of the Americas: Shallow Subduction, Plateau Uplift and Ridge and Terrane Collision*, pp. 229–260, eds Kay, S.M., Ramos, V.A. & Dickinson, W.M., Geological Society of America Memoir 204.

Kay, S.M., Coira, B. & Viramonte, J., 1994. Young mafic back arc volcanic rocks as indicators of continental lithospheric delamination beneath the Argentine Puna Plateau, central Andes, *J. Geophys. Res.,* **99,** 24 323–24 339.

Kennett, B.L. & Engdahl, E.R., 1991. Traveltimes for global earthquake locations and phase identification, *Geophys. J. Int.,* **105,** 429–465.

Kirby, S.H., Stein, S., Okal, E.A. & Rubie, D.C., 1996. Metastable mantle phase transformations and deep earthquakes in subducting oceanic lithosphere, *Rev. Geophys.,* **34,** 261–306.

Knezevic Antonijevic, S., Wagner, L.S., Kumar, A., Beck, S.L., Long, M.D., Zandt, G., Tavera, H. & Condori, C., 2015. The role of ridges in the formation and longevity of flat slabs, *Nature*, in press, doi:10.1038/nature14648.

Koulakov, I., Sobolev, S.V. & Asch, G., 2006. P- and S-velocity images of the lithosphere-asthenosphere system in the Central Andes from local-source tomographic inversion, *Geophys. J. Int.,* **167,** 106–126.

Kumar, A., Wagner, L.S., Beck, S.L., Zandt, G. & Long, M.D., 2014. Imaging Lithospheric-scale Structure Beneath Northern Altiplano in Southern Peru and Northern Bolivia, in *Proceedings of the AGU Fall Meeting*, San Francisco, Abstract T21E–2626.

Lamb, S., 2011. Did shortening in thick crust cause rapid Late Cenozoic uplift in the northern Bolivian Andes?, *J. Geol. Soc.,* **168,** 1079–1092.

Li, C., van der Hilst, R.D., Engdahl, E.R. & Burdick, S., 2008. A new global model for *P* wave speed variations in Earth's mantle, *Geochem. Geophys. Geosyst.,* **9,** Q05018, doi:10.1029/2007GC001806.

Li, X., Kind, R., Yuan, X., Wölbern, I. & Hanka, W., 2004. Rejuvenation of the lithosphere by the Hawaiian plume, *Nature,* **427,** 827–829.

Marot, M., Monfret, T., Gerbault, M., Nolet, G., Ranalli, G. & Pardo, M., 2014. Flat versus normal subduction zones: a comparison based on 3-D regional traveltime tomography and petrological modeling of central Chile and western Argentina (29°-35°S), *Geophys. J. Int.,* **199,** 1633–1654.

Martinod, J., Guillaume, B., Espurt, N., Faccenna, C., Funiciello, F. & Regard, V., 2013. Effect of aseismic ridge subduction on slab geometry and overriding plate deformation: insights from analogue modeling, *Tectonophysics,* **588,** 39–55.

McGeary, S., Nur, A. & Ben-Avraham, Z., 1985. Spatial gaps in arc volcanism: the effect of collision or subduction of oceanic plateaus, *Tectonophysics,* **119,** 195–221.

McQuarrie, N., Horton, B., Zandt, G., Beck, S. & DeCelles, P., 2005. Lithospheric evolution of the Andean fold-thrust belt, Bolivia, and the origin of the Central Andean Plateau, *Tectonophysics,* **399,** 15–37.

Müller, R.D., Sdrolias, M., Gaina, C. & Roest, W.R., 2008. Age, spreading rates, and spreading asymmetry of the world's ocean crust, *Geochem. Geophys. Geosyst.,* **9,** Q04006, doi:10.1029/2007GC001743.

Myers, S., Beck, S., Zandt, G. & Wallace, T., 1998. Lithospheric-scale structure across the Bolivian Andes from tomographic images of velocity and attenuation for P and S waves, *J. Geophys. Res.,* **103,** 21 233–21 252.

Nakajima, J., Matsuzawa, T., Hasegawa, A. & Zhao, D., 2001. Three-dimensional structure of V_p, V_s, and V_p/V_s beneath northeastern Japan: implications for arc magmatism and fluids, *J. Geophys. Res.,* **106**(B10), 21 843–21 857.

Oncken, O., Hindle, D., Kley, J., Elger, K., Victor, P. & Schemmann, K., 2006. Deformation of the central Andean upper plate system – Facts, fiction, and constraints for plateau models, in *The Andes – Active Subduction Orogeny*, pp. 3–27, eds Oncken, O., Chong, G., Franz, G., Giese, P., Götze, H.-J., Ramos, V.A., Strecker, M.R. & Wigger, P., Springer-Verlag, Berlin.

Paige, C. & Saunders, M.A., 1982. LSQR: an algorithm for sparse linear equations and sparse least squares, *ACM Trans. Math. Softw.,* **8,** 43–71.

Pavlis, G. & Vernon, F., 2010. Array processing of teleseismic body waves with the USArray, *Comput. Geosci.,* **36,** 910–920.

Phillips, K. & Clayton, R.W., 2014. Structure of the subduction transition region from seismic array data in southern Peru, *Geophys. J. Int.,* **196,** 1889–1905.

Phillips, K. *et al.*, 2012. Structure of the subduction system in southern Peru from seismic array data, *J. Geophys. Res.,* **117,** B11306, doi:10.1029/2012JB009540.

Porter, R., Gilbert, H., Zandt, G., Beck, S.L., Warren, L., Calkins, J., Alvarado, P. & Anderson, M., 2012. Shear wave velocities in the Pampean flat-slab region from Rayleigh wave tomography: implications for slab and upper mantle hydration, *J. Geophys. Res.,* **117,** B11301, doi:10.1029/2012JB009350.

Ray, J.S., Mahoney, J.J., Duncan, R.A., Ray, J., Wessel, P. & Naar, D.F., 2012. Chronology and geochemistry of lavas from the Nazca Ridge and Easter Seamount Chain: an ~30 Myr hotspot record, *J. Petrol.,* **53,** 1417–1448.

Ribe, N.M., Stutzmann, E., Ren, Y. & van der Hilst, R., 2007. Buckling instabilities of subducted lithosphere beneath the transition zone, *Earth planet. Sci. Lett.,* **254,** 173–179.

Rosenbaum, G., Giles, D., Saxon, M., Betts, P., Weinberg, R. & Duboz, C., 2005. Subduction of the Nazca Ridge and the Inca Plateau: insights into the formation of ore deposits in Peru, *Earth planet. Sci. Lett.,* **239,** 18–32.

Ryan, J., Beck, S.L., Zandt, G., Wagner, L., Minaya, E. & Tavera, H., 2012. The under-side of the Andes: using receiver functions to map the north central Andean subsurface, in *Proceedings of the AGU Fall Meeting*, San Francisco, Abstract T21E–2626.

Saylor, J.E. & Horton, B.K., 2014. Nonuniform surface uplift of the Andean plateau revealed by deuterium isotopes in Miocene volcanic glass from southern Peru, *Earth planet. Sci. Lett.,* **387,** 120–131.

Schmandt, B. & Humphreys, E., 2010. Seismic heterogeneity and small-scale convection in the southern California upper mantle, *Geochem. Geophys. Geosyst.,* **11,** Q05004, doi:10.1029/2010GC003042.

Schneider, J.F. & Sacks, L.S., 1987. Stress in the contorted Nazca Plate beneath southern Peru from local earthquakes, *J. Geophys. Res.,* **92**(B13), 13 887–13 902.

Schurr, B., Rietbrock, A., Asch, G., Kind, R. & Oncken, O., 2006. Evidence for lithospheric detachment in the central Andes from local earthquake tomography, *Tectonophysics,* **415,** 203–223.

Scire, A., Biryol, C., Zandt, G. & Beck, S., 2015. Imaging the Nazca slab and surrounding mantle to 700 km depth beneath the Central Andes (18° to 28°S), in *Geodynamics of a Cordilleran Orogenic System: The Central Andes of Argentina and Northern Chile*, pp. 23–41, eds DeCelles, P.G., Ducea, M.N., Carrapa, B. & Kapp, P., Geological Society of America Memoir 212.

Siebert, L. & Simkin, T., 2002. *Volcanoes of the world: an illustrated catalog of Holocene volcanoes and their eruptions*, Smithsonian Institution, Global Volcanism Program Digital Information Series, GVP-3. Available at: http://volcano.si.edu/search_volcano.cfm (last accessed 4 June 2014).

Skinner, S.M. & Clayton, R.W., 2013, The lack of correlation between flat slabs and bathymetric impactors in South America, *Earth planet. Sci. Lett.,* **371–372,** 1–5.

Snoke, J.A., Sacks, I.S. & Okada, H., 1977. Determination of the subducting lithosphere boundary by use of converted phases, *Bull. seism. Soc. Am.,* **67,** 1051–1060.

Sodoudi, F., Yuan, X., Asch, G. & Kind, R., 2011. High-resolution image of the geometry and thickness of the subducting Nazca lithosphere beneath northern Chile, *J. Geophys. Res.,* **116,** B04302, doi:10.1029/2010JB007829.

Somoza, R. & Ghidella, M.E., 2012. Late Cretaceous to recent plate motion in western South America revisited, *Earth planet. Sci. Lett.,* **331–332,** 152–163.

Swenson, J.L, Beck, S.L. & Zandt, G., 2000. Crustal structure of the Altiplano from broadband regional waveform modeling: implications for the composition of thick continental crust, *J. Geophys. Res.,* **105,** 607–621.

Tassara, A., 2005. Interaction between the Nazca and South American plates and formation of the Altiplano-Puna Plateau: review of a flexural analysis along the Andean margin (15°–34°S), *Tectonophysics,* **399,** 39–57.

Tassara, A., Swain, C., Hackney, R. & Kirby, J., 2007. Elastic thickness structure of South America estimated using wavelets and satellite-derived gravity data, *Earth planet. Sci. Lett.,* **253,** 17–36.

VanDecar, J.C. & Crosson, R.S., 1990. Determination of teleseismic relative phase arrival times using multi-channel cross-correlation and least squares, *Bull. seism. Soc. Am.,* **80,** 150–169.

van Hunen, J., van der Berg, A.P. & Vlaar, N.J., 2002. The impact of the South-American plate motion and the Nazca Ridge subduction on the flat subduction below Peru, *Geophys. Res. Lett.,* **29,** 1690, doi:10.1029/2001GL014004.

van Hunen, J., van der Berg, A.P. & Vlaar, N.J., 2004. Various mechanisms to induce present-day shallow flat subduction and implications for the younger Earth: a numerical parameter study, *Phys. Earth planet. Int.,* **146,** 179–194.

von Huene, R., Pecher, I. & Gutscher, M.-A., 1996. Development of the accretionary prism along Peru and material flux after subduction of the Nazca Ridge, *Tectonics,* **15,** 19–33.

Wagner, L.S., Beck, S.L. & Long, M.D., 2010. PerU Lithosphere and Slab Experiment, Other/Seismic Network, International Federation of Digital Seismograph Networks, doi:10.7914/SN/ZD_2010.

Ward, K., Porter, R.C., Zandt, G., Beck, S.L., Wagner, L.S., Minaya, E. & Tavera, H., 2013. Ambient noise tomography across the central Andes, *Geophys. J. Int.,* **194,** 1559–1573.

Ward, K., Porter, R.C., Zandt, G., Beck, S.L., Wagner, L.S., Minaya, E. & Tavera, H., 2014. Erratum: ambient noise tomography across the central Andes, *Geophys. J. Int.,* **196,** 1264–1265.

Whitman, D., Isacks, B.L. & Kay, S.M., 1996. Lithospheric structure and along-strike segmentation of the Central Andean Plateau: seismic Q, magmatism, flexure, topography and tectonics, *Tectonophysics,* **259,** 29–40.

Wiens, D.A., 2001. Seismological constraints on the mechanism of deep earthquakes: temperature dependence of deep earthquake source properties, *Phys. Earth planet. Int.,* **127,** 145–163.

Wölbern, I., Heit, B., Yuan, X., Asch, G., Kind, R., Viramonte, J., Tawackoli, S. & Wilke, H., 2009. Receiver function images from the Moho and the slab beneath the Altiplano and Puna Plateaus in the Central Andes, *Geophys. J. Int.,* **177,** 296–308.

Woods, M.T. & Okal, E.A., 1994. The structure of the Nazca ridge and Sala y Gomez seamount chain from the dispersion of Rayleigh waves, *Geophys. J. Int.,* **117,** 205–222.

Yuan, X. *et al.*, 2000. Subduction and collision processes in the Central Andes constrained by converted seismic phases, *Nature,* **408,** 958–961.

Yuan, X., Sobolev, S.V. & Kind, R., 2002. Moho topography in the central Andes and its geodynamic implications, *Earth planet. Sci. Lett.,* **199,** 389–402.

Zandt, G., Beck, S.L., Ruppert, S.R., Ammon, C.J., Rock, D., Minaya, E., Wallace, T.C. & Silver, P.G., 1996. Anomalous crust of the Bolivian Altiplano, central Andes: constraints from broadband regional seismic waveforms, *Geophys. Res. Lett.,* **23,** 1159–1162.

Zhao, D., 2004. Global tomography images of mantle plumes and subducting slabs: insights into deep Earth dynamics, *Phys. Earth planet. Inter.,* **146,** 3–24.

Zhao, D., Yamamoto, Y. & Yanada, T., 2013. Global mantle heterogeneity and its influence on teleseismic regional tomography, *Gondwana Res.*, **23,** 595–616.

SUPPORTING INFORMATION

Additional Supporting Information may be found in the online version of this paper:

Table S1. Slab contours for the subducting Nazca slab from 8 to 20 degrees S determined from this study using constraints discussed in the text. The contours are shown in Figure 12a.

Figure S1. Normalized hit quality plots for *P*-wave tomography model. Black stars on 95 km depth layer are station locations. Hit quality for a node is based on the number and azimuthal distribution of rays that sample that node. Good hit quality is indicated by red shading while poor hit quality is indicated by blue shading. Hit quality is strongly controlled by station distribution in uppermost depth slices with decreasing dependence on station distribution as depth increases.

Figure S2. Normalized hit quality plots for *S*-wave tomography model. Black stars on 95 km depth layer are station locations. Hit quality for a node is based on the number and azimuthal distribution of rays that sample that node. Good hit quality is indicated by red shading while poor hit quality is indicated by blue shading. Hit quality is strongly controlled by station distribution in uppermost depth slices with decreasing dependence on station distribution as depth increases.

Figure S3. Plot of trade-off analysis for the *P*-wave inversion between the variance reduction and the Euclidean model norm (L2) performed to choose preferred overall damping (D1–D10) and smoothing (S1–S10) weights. The black star shows the damping (D6) and smoothing (S5) parameters used in this study.

Figure S4. Horizontal depth slices for the checkerboard tests for a selection of model layers. Input for neutral layers (0 per cent velocity deviation) is not shown. Output for neutral layers is shown in the left column. The short dashed line represents the edge of the well-resolved region of the model, defined as regions with hit quality greater than 0.2 (Biryol *et al.* 2011). (A) Checkerboard tests for *P*-wave inversion. The checkerboard tests show that for shallower layers, resolution is controlled by station distribution as expected. Deeper model layers indicate that while the input amplitude cannot be completely resolved, lateral changes in anomalous velocity resolve with little horizontal smearing. Resolution is lost towards the edges of the model region. Resolution of velocity anomalies in neutral layers shown here (left column) indicates that some vertical smearing is occurring. (B) Checkerboard tests for *S*-wave inversion. Larger input 'checkers' are used for *S*-waves due to decreased resolution of *S*-wave inversion relative to *P*-wave inversion. Amplitude recovery for the *S*-wave inversion decreases more rapidly with depth than for the *P*-wave inversion. Resolution of velocity anomalies in neutral layers shown here (left column) indicates that some vertical smearing is occurring.

Figure S5. E–W oriented cross-sections through checkerboard tests for *S*-wave inversion. Dashed lines are the same as in Fig. S4. Irregular distribution of anomalies with depth in synthetic input (left) is due to the dilation of the node spacing with depth. Location of cross-sections shown in map in lower left.

Figure S6. Cross-section results for our synthetic anomaly recovery tests for *S*-wave inversion. Cross-section locations are shown in Fig. 1. Dashed lines are the same as in Fig. S4. The geometry of our input slab model is based on the Slab1.0 contours (black line, Hayes *et al.* 2012). Labelled anomalies (C, D and E) based on output from tomographic inversion. Synthetic input (left) and recovered Vs (right) models are shown. Decreased amplitude recovery and vertical smearing of the recovered slab anomaly is observed in the upper 200 km of the model. In general, the amplitude recovery increases with depth.

Figure S7. Depth slices for our synthetic anomaly recovery tests for *P*-wave inversion. Dashed lines are the same as in Fig. S4. The geometry of our input slab model is based on the Slab1.0 contours (Hayes *et al.* 2012). Labelled anomalies (C, D and E) based on output from tomographic inversion. Synthetic input (left) and recovered Vp (right) models are shown.

Figure S8. Depth slices for our synthetic anomaly recovery tests for *S*-wave inversion. Dashed lines are the same as in Fig. S4. The geometry of our input slab model is based on the Slab1.0 contours (Hayes *et al.* 2012). Labelled anomalies (C, D and E) based on output from tomographic inversion. Synthetic input (left) and recovered Vs (right) models are shown.

Figure S9. Horizontal depth slices for 240 and 320 km from the tomography model for both Vp (left) and Vs (right). The short dashed line represents the edge of the well-resolved region of the model, defined as regions with hit quality greater than 0.2 (Biryol *et al.* 2011). Red triangles mark location of Holocene volcanoes (Siebert & Simkin 2002). Yellow dots are earthquake locations from the EHB catalogue (Engdahl *et al.* 1998). Solid black lines are slab contours from Slab1.0 model (Hayes *et al.* 2012). Heavy black outline marks the projection of the subducted Nazca Ridge from Hampel (2002). Labelled anomalies (A, D and E) are discussed in the text.

Figure S10. Horizontal depth slices for 455, 555 and 660 km from the tomography model for both Vp (left) and Vs (right). Dashed lines are the same as in Fig. S9. Red triangles mark location of Holocene volcanoes (Siebert & Simkin 2002). Yellow dots are earthquake locations from the EHB catalogue (Engdahl *et al.* 1998). Solid black lines are slab contours from Slab1.0 model (Hayes *et al.* 2012).

Figure S11. Trench parallel cross-sections through the Vs tomography model. Cross-section locations are as shown in Fig. 1. Dashed lines are the same as in Fig. S9. Intersection with trench perpendicular cross-sections indicated by italicized letters A, B, C and D. Yellow dots are earthquake locations from the EHB catalogue (Engdahl *et al.* 1998). Solid black line marks the top of the Nazca slab from the Slab1.0 model (Hayes *et al.* 2012). Orange dots mark reflection points from James & Snoke (1990). Labelled anomalies (A, C, D and E) are discussed in the text (http://gji.oxfordjournals.org/lookup/suppl/doi:10.1093/gji/ggv452/-/DC1).